

LIGHTING THE DARK MOLECULAR GAS: H₂ AS A DIRECT TRACER

ADITYA TOGI¹ AND J. D. T. SMITH¹

Draft version May 15, 2018

ABSTRACT

Robust knowledge of molecular gas mass is critical for understanding star formation in galaxies. The H₂ molecule does not emit efficiently in the cold interstellar medium, hence the molecular gas content of galaxies is typically inferred using indirect tracers. At low metallicity and in other extreme environments, these tracers can be subject to substantial biases. We present a new method of estimating total molecular gas mass in galaxies directly from pure mid-infrared rotational H₂ emission. By assuming a power-law distribution of H₂ rotational temperatures, we can accurately model H₂ excitation and reliably obtain warm ($T \gtrsim 100$ K) H₂ gas masses by varying only the power law's slope. With sensitivities typical of Spitzer/IRS, we are able to directly probe the H₂ content via rotational emission down to ~ 80 K, accounting for $\sim 15\%$ of the total molecular gas mass in a galaxy. By extrapolating the fitted power law temperature distributions to a calibrated *single* lower cutoff temperature, the model also recovers the total molecular content within a factor of ~ 2.2 in a diverse sample of galaxies, and a subset of broken power law models performs similarly well. In ULIRGs, the fraction of warm H₂ gas rises with dust temperature, with some dependency on α_{CO} . In a sample of five low metallicity galaxies ranging down to $12 + \log[\text{O}/\text{H}] = 7.8$, the model yields molecular masses up to $\sim 100\times$ larger than implied by CO, in good agreement with other methods based on dust mass and star formation depletion timescale. This technique offers real promise for assessing molecular content in the early universe where CO and dust-based methods may fail.

Subject headings: ISM:molecules—galaxies:ISM—infrared:ISM

1. INTRODUCTION

By a factor of more than 10^4 , H₂ is the most abundant molecule in the universe, found in diverse environments ranging from planet atmospheres to quasars hosts (Hanel et al. 1979, 1981; Walter et al. 2003; Genzel et al. 2015). It was the first neutral molecule to form in the Universe and hence dominated the cooling of pristine gas at early times (Lepp et al. 2002). Stars form principally from molecular clouds, and most physical prescriptions for stellar formation rate (SFR) are therefore directly linked to the surface density of H₂ gas (Kennicutt 1998; Bigiel et al. 2008). To understand the star formation processes and how it varies and has evolved over the star-forming history of the Universe, it is necessary to accurately measure the mass and distribution of H₂.

Despite its high abundance, H₂ can be difficult to study directly. It possess no permanent dipole moment, which makes it a weak rotational emitter. In addition, the upper energy level for the lowest permitted rotational (quadrupole) transition is $E/k = 510$ K above ground (Dabrowski 1984; van Dishoeck & Black 1986). Hence, the H₂ gas that comprises the bulk of the molecular interstellar medium (ISM) is commonly believed to be too cold to be visible. And yet, despite these observational disadvantages, the advent of the Infrared Space Observatory (ISO) and in particular Spitzer's Infrared Spectrograph (IRS, Houck et al. 2004) revealed pure rotational H₂ emission from a rich variety of extragalactic sources, including normal star forming galaxies (Roussel et al. 2007), ultraluminous and luminous infrared galaxies (U/LIRGs Lutz et al. 2003; Pereira-Santaella 2010;

Veilleux et al. 2009; Stierwalt et al. 2014), galaxy mergers (Appleton et al. 2006), radio-loud AGN (Ocaña Flaquer et al. 2010), UV-selected galaxies (O'Dowd et al. 2009), quasar hosts (Evans et al. 2001), cooling-flow cluster systems (Egami et al. 2006), sources with extreme shock-dominated energetics (Ogle et al. 2010), and even star-forming sources at redshifts $\gtrsim 2$ (Ogle et al. 2012).

In the absence of direct measurements of H₂, the lower rotational line transitions of CO (the next most abundant molecule) are generally used as a molecular gas tracer. To convert the measured integrated intensities of ¹²CO to H₂ column density a conversion factor, α_{CO} , is needed, typically calibrated against virial mass estimates in presumed self-gravitating clouds (Solomon et al. 1987; Scoville et al. 1987; Strong & Mattox 1996; Abdo et al. 2010). However recent evidence indicates that the value of α_{CO} varies substantially, both within galaxies and at different epochs (Genzel et al. 2012; Sandstrom et al. 2013).

In molecular clouds in our Galaxy, the observed γ -ray flux arising from the cosmic ray interactions with H₂ can be used to recover H₂ gas mass accurately (Bhat et al. 1985; Bloemen et al. 1984, 1986), but this method requires information on the cosmic ray distribution not available in other galaxies. Another method to assess H₂ content is to use dust as a tracer, with a presumed or recovered dust-to-gas (DGR) ratio (e.g. Sandstrom et al. 2013; Rémy-Ruyer et al. 2014). Among other biases, both the CO and dust-based methods lose reliability at low metallicity. Due to declining dust opacity and less effective self-shielding than H₂, the CO abundance drops rapidly with decreasing metallicity (Wolfire et al. 2010; Bolatto et al. 2013). Variations in the radiation field can also lead to selective CO destruction (Hudson 1971; Bolatto et al. 2013). At the lowest metallicities, DGR itself

¹ Ritter Astrophysical Research Center, University of Toledo, 2825 West Bancroft Street, M. S. 113, Toledo, OH 43606
Email: aditya.togi@utoledo.edu

begins to scale non-linearly with the metal content of the gas (Herrera-Camus et al. 2012; Fisher et al. 2014; Rémy-Ruyer et al. 2014). Another method of inferring molecular gas content is to couple measured star formation rates with an assumed constant H₂ depletion timescale (τ_{dep}), equivalent to a constant star formation efficiency (SFE) in galaxies (Schruba et al. 2012). None of these methods provide *direct* tracers of the H₂ reservoirs, and the relevant indirect tracers all rely on physical assumptions (e.g. constant or measurable values of α_{CO} , DGR, or τ_{dep}) which are unlikely to be valid in all environments.

Here we challenge the long-stated assumption that H₂ rotational emission is a poor tracer of the total molecular content in galaxies. Our understanding of the structure of the molecular material in galaxies is undergoing significant revision. While CO traces the coldest component of the molecular ISM, half or more (and sometimes much more) of the molecular gas in galaxies is in a warmer, CO-dark state, where H₂ persists (Field et al. 1966; Tielens 2005; Draine 2011; Wolfire et al. 2010; Pineda et al. 2013; Velusamy & Langer 2014). What this means is that the common wisdom that all molecular gas is found at temperatures $T = 10 - 20$ K is incorrect. With molecular material existing in quantity at excitation temperatures 50 - 100 K, it becomes possible to use the rotational emission spectrum of the Universe’s dominant molecule to directly assess a substantial portion of the total molecular content in galaxies.

We introduce here a simple continuous temperature model which enables direct use of the H₂ rotational emission from galaxies to recover their total molecular gas content. While several assumptions are required to make such a model possible, the resulting biases are expected to be completely distinct from those of the indirect gas tracers. The paper is laid out as follows. We describe the archival sample in § 2. A rotational temperature distribution model is presented in § 3, and in § 4 we describe the method and its calibration procedure. Section 5 presents results, discussions, applications and future prospects of our model. We summarize our conclusions in § 6.

2. SAMPLE

We have selected a large sample of galaxies spanning a wide range of different physical properties with reliable H₂ rotational emission detections. Our sample includes 14 Low Ionization Nuclear Emission Regions (LINERs), 18 galaxies with nuclei powered by star formation, 6 Seyfert galaxies, 5 dwarf galaxies, 11 radio galaxies, 19 Ultra Luminous Infrared galaxies (ULIRGs), 9 Luminous Infrared galaxies (LIRGs), and 1 Quasi Stellar Object (QSO) host galaxy. The galaxies were chosen to have at least three well-detected H₂ pure-rotational lines with Spitzer/IRS (Houck et al. 2004), including either S(0) or S(1), occurring at 28.22 and 17.04 μm , respectively. We also required an available measurements of CO line emission (either J = 1–0 or 2–1) for an alternative estimate of the total molecular gas mass. See Table 1 for a complete sample list with relevant physical parameters and the references from which each galaxy was drawn.

The flux ratios S_{70}/S_{160} are calculated using 70 and 160 μm intensities obtained from the *Herschel*-PACS instrument (Poglitsch et al. 2010). We convolved PACS 70 μm maps to the lower resolution of PACS 160 μm to calculate flux ratios for mapped regions, for which we

have the H₂ line flux. For ULIRGs and other unresolved galaxies, S_{70}/S_{160} represents the global flux ratio. The PACS70/PACS160 ratios are listed in Table 1 for each galaxy.

2.1. MIR H₂ rotational line fluxes

All MIR H₂ rotational line fluxes were obtained from *Spitzer*-IRS observations at low ($R \sim 60 - 120$) and high ($R \sim 600$) resolution between 5 - 38 μm . The Spitzer Infrared Nearby Galaxies Survey (SINGS, Kennicutt et al. 2003) is a diverse sample of nearby galaxies spanning a wide range of properties. The SINGS sample consists of LINERs, Seyferts, dwarfs, and galaxies dominated by star formation in their nuclei. We adopted the H₂ rotational line fluxes for four lowest rotational lines (S(0) to S(3)) in SINGS galaxies from Roussel et al. (2007). The targets were observed in spectral mapping mode and the details of the observing strategy is described in Kennicutt et al. (2003) and Smith et al. (2004).

H₂ rotational line fluxes for 10 3C radio galaxies are from Ogle et al. (2010). This sample includes from S(0) to S(7). For the radio galaxy 3C 236, the fluxes of H₂ rotational lines are obtained from Guillard et al. (2012).

The H₂ rotational line fluxes for QSO PG 1440+356 were taken from the Spitzer Quasar and ULIRG Evolution Study (QUEST) sample of Veilleux et al. (2009), and those for the 19 ULIRGs were obtained from Higdon et al. (2006). The fluxes of H₂ rotational lines for the NGC 6240 and other LIRGs in the sample are from Armus et al. (2006) and Pereira-Santaella (2010), respectively. H₂ rotational lines are also observed in the molecular outflow region of NGC 1266 (Alatalo et al. 2011). Table 2 lists the flux of MIR H₂ rotational lines for all our selected galaxies.

2.2. Cold molecular gas mass from CO line intensities

To test and calibrate a model which measures total molecular mass from the rotational lines of H₂, an estimate of the “true” cold H₂ gas mass in a subset of galaxies is required. For this purpose, we utilize the cold H₂ gas masses for the SINGS sample compiled by Roussel et al. (2007), which are derived from aperture-matched CO velocity integrated intensities. The observed line intensities of the 2.6 mm ¹²CO(1–0) line within the measured CO beam size was chosen to match the aperture of the *Spitzer*-IRS spectroscopic observations. Roussel et al. (2007) assumed a CO intensity to molecular gas conversion factor (α_{CO}) of $5.0 M_{\odot} (\text{K km s}^{-1} \text{ pc}^2)^{-1}$ (equivalent to $X_{CO} = 2.3 \times 10^{20} \text{ cm}^{-2} (\text{K km s}^{-1})^{-1}$). They applied aperture corrections by projecting the IRS beam and CO beam on the 8 μm *Spitzer*-IRAC map. The underlying assumption is that the spatial distribution of the aromatic band in emission and CO(1–0) line emission are similar at large spatial scales.

For the radio galaxies, molecular gas masses were compiled by Ogle et al. (2010), and the molecular gas mass was estimated from the CO flux density corrected and scaled to the standard Galactic CO conversion factor. For the radio galaxy 3C 236 Ocaña, Flaquer et al. (2010) estimated an upper limit to the cold H₂ gas mass. The cold H₂ gas masses for the LIRGs in our sample were obtained from Sanders et al. (1991). They used $\alpha_{CO} = 6.5 M_{\odot} (\text{K km s}^{-1} \text{ pc}^2)^{-1}$ (equivalent to $X_{CO} = 3.0 \times 10^{20} \text{ cm}^{-2} (\text{K km s}^{-1})^{-1}$). We derived aperture corrections

to the CO intensities by projecting IRS and CO beam on the 8 μm IRAC map, since the CO beam size (55'' aperture) is much larger than the IRS mapped region (13.4'' \times 13.4''). Required aperture corrections are typically less than a factor of 2. For the LIRGs NGC 7591, NGC 7130, and NGC 3256, the value of molecular gas mass was obtained from Lavezzi & Dickey (1998); Curran et al. (2000); Sakamoto et al. (2006), respectively. The global molecular gas masses for ULIRGs are from Rigopoulou et al. (1996); Sanders et al. (1991); Mirabel et al. (1989); Evans et al. (2002). For the quasar QSO PG 1440+356 Evans et al. (2001) derived the molecular gas mass.

Different studies have utilized substantially different α_{CO} values to calculate molecular gas masses. In the Milky Way disk, a modern value of $\alpha_{\text{CO,Gal}} = 4.35 \pm 1.3 M_{\odot}(\text{K km s}^{-1} \text{pc}^2)^{-1}$ (equivalent to $X_{\text{CO}} = 2.0 \times 10^{20} \text{cm}^{-2}(\text{K km s}^{-1})^{-1}$) has been found to be consistent with a wide variety of constraints (Bolatto et al. 2013). In this work, we scale all molecular gas mass estimates to correspond to $\alpha_{\text{CO}} = \alpha_{\text{CO,Gal}}$. Since we require only the H_2 gas masses in our analysis, the resulting molecular mass values were further reduced by a factor of 1.36 to remove the mass contribution of Helium and other heavy elements. Recent dust-based studies of a subset of the SINGS sample have revealed variations in α_{CO} both between and within these galaxies Sandstrom et al. (2013).

Table 2 lists the CO-based H_2 gas mass estimated for each galaxy in the sample, aperture matched to the region of Spitzer/IRS coverage, along with H_2 masses calculated using the conversion factor for central regions derived by Sandstrom et al. (2013) in parentheses, where available.

3. MODEL

The primary methods of measuring H_2 mass all rely on a set of assumptions — that the α_{CO} factor is known and constant, that the dust-to-gas ratio is fixed or tied directly to metallicity, or that the star formation depletion time is unchanged from environment to environment. All of these methods also rely on indirect tracers: the CO molecule, which is 10,000 \times less abundant than H_2 , dust grains, with their complex formation and destruction histories and varying illumination conditions, or newly formed stars, which are presumed to be associated with molecular material with a consistent conversion efficiency. All of these methods suffer biases based on the physical assumptions made.

We propose a *direct* means of assessing total molecular gas mass using the MIR quadrupole rotational line emission of H_2 . Interstellar or direct ultraviolet radiation fields, shocks, and other mechanical heating processes are all potential sources of H_2 excitation. The method we propose requires only the assumption that H_2 rotational temperatures are, when averaged over the diversity of emitting environments and processes in galaxies, widely distributed, and smoothly varying. This is directly analogous to modeling the radiation field intensity which heats dust grain populations in galaxies with a smooth distribution (e.g. Draine et al. 2007; Galliano et al. 2003). We model the H_2 temperature distribution as a smooth, truncated **power law** with fixed cutoff temperatures. Indeed, the H_2 molecule is radiatively cooled by a cooling function which can be well approximated as

a power law with slope 3.8 (Hollenbach & McKee 1979; Draine & McKee 1993). A similar analysis by Burton (1987) derived a cooling function with a power law index, $n = 4.66$, for H_2 molecules in the temperature range 10–2000 K.

The temperature equivalents of H_2 rotational levels are high, starting at $T = 510$ K (see Table 3). The Boltzmann distribution of energy levels, however, leads to substantial excitation even at more modest peak temperatures. The lowest upper energy levels at $J = 2-4$ are well populated at excitation temperatures of 50 to 150 K, whereas the higher- J levels are excited by temperatures from a few hundred to several hundred K. Typically, a small number of discrete temperature components are fitted to low- J rotational line fluxes, recovering warm H_2 temperatures in this range (Spitzer et al. 1973; Spitzer & Cochran 1973; Spitzer et al. 1974; Spitzer & Zweibel 1974; Savage et al. 1977; Valentijn & van der Werf 1999; Rachford et al. 2002; Browning et al. 2003; Snow & McCall 2006; Ingalls et al. 2011).

Other studies have also adopted continuous temperature distributions for H_2 . Zakamska (2010) in her study of H_2 emission in ULIRGs used a power law model $dM \propto T^{-n}dT$ to calculate the expected H_2 rotational line ratios, where dM is the mass of H_2 gas with excitation temperatures between T and $T + dT$. In her sample, power law indices $2.5 < n < 5.0$ are required to reproduce the observed range of H_2 line ratios. Similarly Pereira-Santaella et al. (2014) adopted a power-law distribution in H_2 to model H_2 rotational emission in six local infrared bright Seyfert galaxies, with power law indexes ranging from 4–5. In the shocked environment of supernova remnant IC 443, Neufeld & Yuan (2008) found a power law temperature distribution for H_2 column density with power law index varying over the range 3–6 with an average value of 4.5.

The present practice for measuring warm ($T \gtrsim 150\text{K}$) H_2 gas mass is to use two or three distinct temperature components to model the H_2 rotational line fluxes. Yet even on the scales of individual molecular clouds, H_2 is present at a wide range of temperatures, calling into question whether discrete temperature components are physical. When used purely for assessing warm gas mass ($T \gtrsim 100\text{K}$), the power law method provides a more robust, unique and reproducible measure than discrete temperature fits, which are sensitive to the arbitrary choice of starting line pair. A continuous distribution also makes possible extrapolation to a suitable lower temperature to recover the total cold molecular gas mass (see § 4).

We fit the flux of H_2 rotational lines using a continuous power law temperature distribution by assuming

$$dN = mT^{-n}dT, \quad (1)$$

where dN is the column density of H_2 gas between excitation temperature T and $T + dT$, n is the power law index, and m is a constant. Integrating this distribution to recover the total column density, the scaling co-efficient m is found to be

$$m = \frac{N_{\text{tot}}(n-1)}{T_{\ell}^{1-n} - T_u^{1-n}}, \quad (2)$$

where T_{ℓ} and T_u are the lower and upper temperatures of the distribution, respectively, and N_{obs} is the column

density of H_2 in the observed line of sight and temperature is presumed equal to the rotational temperature. For a continuous distribution of molecules with respect to temperature, the column density of molecules at upper energy level j responsible for the transition line $S(j)$ is

$$N_j = \int_{T_\ell}^{T_u} \frac{g_j}{Z(T)} \times e^{-\frac{E_j}{kT}} m T^{-n} dT, \quad (3)$$

where g_j is the degeneracy value for the corresponding energy level E_j . The degeneracy value for even and odd values of j corresponding to para and ortho H_2 is

$$g_j = 2j + 1, \quad (4)$$

and

$$g_j = 3(2j + 1), \quad (5)$$

respectively. The factor of 3 for odd values of j is for ortho-hydrogen, which have parallel proton and electron spins, forming a triplet state. $Z(T)$ is the partition function at temperature T . The model assumes local thermodynamic equilibrium (LTE) between ortho and para H_2 and the abundance ratio of ortho to para H_2 at any temperature, T , in LTE is given by Burton et al. (1992). The partition functions for para and ortho H_2 are

$$Z(T) = Z_p(T) = \sum_{j=even}^{\infty} (2j + 1) e^{-\frac{E_j}{kT}} \quad (6)$$

and

$$Z(T) = Z_o(T) = \sum_{j=odd}^{\infty} 3(2j + 1) e^{-\frac{E_j}{kT}}, \quad (7)$$

respectively.

Table 3 list the wavelength of each H_2 rotational line transition, the upper energy level of the corresponding transition in temperature units, and their radiative rate coefficients A (Huber 1979; Black & Dalgarno 1976).

Assuming H_2 emission to be optically thin, the flux observed in a given transition j is

$$F_j = \frac{h\nu AN_{j+2}\Omega}{4\pi}, \quad (8)$$

where Ω is the solid angle of the observation. Substituting the value of N_j from equation 3 into Eq. 8 and then using equation 2, we obtain the total column density

$$N_{tot} = \frac{4\pi F_j \lambda (T_\ell^{1-n} - T_u^{1-n})}{A h c \Omega (n-1) \int_{T_\ell}^{T_u} \frac{g_{j+2}}{Z(T)} e^{-\frac{E_{j+2}}{kT}} T^{-n} dT} \quad (9)$$

From Eq. 8, we conclude that the column density is proportional to the flux F and the corresponding transition wavelength λ , and inversely proportional to the spontaneous emission probability A ,

$$N_{j+2} \propto \frac{F_j \lambda}{A} \quad (10)$$

To perform the fit, we develop an excitation diagram from the ratio of column densities,

$$\frac{N_{j+2}}{N_3} = \frac{F_j \lambda_j A_1}{F_1 \lambda_1 A_j}, \quad (11)$$

where N_3 is the column density of the upper energy level of the transition S(1). We select N_3 , corresponding to the S(1) transition, since it is the brightest and most frequently detected line. Using equation 3, we find this column density ratio from the continuous temperature model to be

$$\frac{N_{j+2}}{N_3} = \frac{\int_{T_\ell}^{T_u} \frac{g_{j+2}}{Z(T)} \times e^{-\frac{E_{j+2}}{kT}} T^{-n} dT}{\int_{T_\ell}^{T_u} \frac{g_3}{Z(T)} \times e^{-\frac{E_1}{kT}} T^{-n} dT}. \quad (12)$$

We determined the parameters of our model by comparing the observed and the modeled column density ratios from equation 11 and 12, by varying the lower temperature T_ℓ and power law index n (the upper temperature, T_u , is fixed, see §4). Knowing these parameters, we substitute their values in equation 9, to obtain the total column density. The total number of molecules is calculated using

$$n_{tot} = N_{tot} \Omega d^2, \quad (13)$$

where n_{tot} is the total number of hydrogen molecules and d is the distance to the object. We then calculate the total H_2 gas mass,

$$M_{H_2, tot} = n_{tot} \times m_{H_2}, \quad (14)$$

where m_{H_2} is the mass of a hydrogen molecule.

4. METHOD & CALIBRATION

Applying the model developed in §3 permits direct assessment of the warm H_2 column. The model-derived lower temperature is typically degenerate, so extrapolating the model to lower temperatures to recover the full molecular content requires a calibration procedure using a trusted independent estimate of H_2 content. Here we describe both applications.

4.1. Warm H_2

The power law temperature distribution of H_2 molecules in Eq.1 has three primary parameters: upper temperature T_u , power law index n , and lower temperature T_ℓ . An excitation diagram formed from the H_2 line flux ratios is the distribution of normalized level populations and constrains our model parameters. Excitation diagrams relate the column density of the upper level (N_u) of a particular transition, normalized by its statistical weight, g_u , as a function of its energy level E_u . In the following sections we describe how the model can be used to estimate the warm H_2 gas mass. In practice, except in a few cases, the lower temperature cutoff T_ℓ is not directly constrained (see §4.2.1). The model fit results themselves are given in Table 4.

4.1.1. Upper temperature, T_u

The bond dissociation energy for H_2 is 4.5 eV, corresponding to $E/k \sim 5 \times 10^4$ K, hence H_2 is not typically bound above this temperature. H_2 present in photodissociation regions (PDRs) in the outer layers of the molecular cloud can reach temperatures of a few 100 K (Hollenbach & Tielens 1997, 1999). For the SINGS galaxies, Roussel et al. (2007) concluded that the mass of H_2 greater than 100 K contributes 1–30% of the total H_2

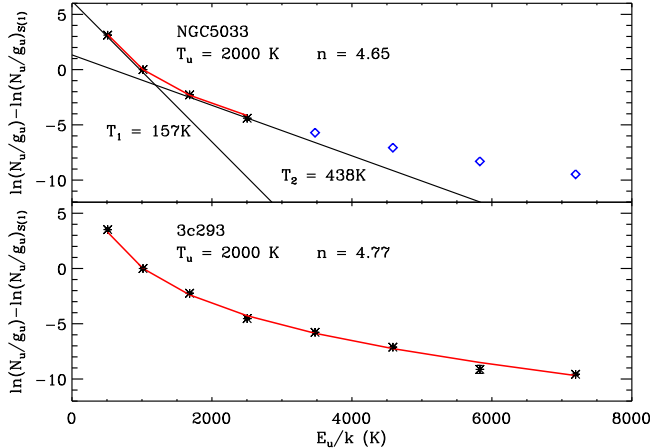


FIG. 1.— Excitation Diagram for NGC 5033 and 3c 293. The N_u/g_u ratios are normalized with respect to the S(1) transition. The solid red line indicates our model fit to the observed normalized columns, denoted by black points. The error bars on the black points are comparable to the symbol sizes. The resulting model parameters T_u , and n are indicated. The two solid lines show the two discrete temperature fit adopted by Roussel et al. (2007). The blue diamonds show model-predicted ratio values for the (unobserved) S(4)–S(7) H_2 rotational lines in NGC 5033. The lower panel for 3c 293 shows our model fit to all the MIR rotational lines S(0)–S(7) detected with the *IRS-Spitzer*. The radio jets in 3c293 shock-excite H_2 to high energy levels resulting in high rotational line fluxes. A single power law model, varying only slope, reproduces H_2 excitation across a wide range of excitation energy.

gas mass. In the MOlecular Hydrogen Emission Galaxies (MOHEGs) of Ogle et al. (2010), $M(H_2) > 1500$ K contributes only 0.01% of the total H_2 . $M(H_2) > 300$ K contributes less than 1% in ULIRGs (Higdon et al. 2006).

In our model, when T_u is allowed to vary above 1000 K, we found negligible impact on the recovered total gas mass or the quality of the fit to the excitation diagram. We therefore fixed the upper temperature of the power law model distribution at $T_u = 2000$ K. H_2 's rovibrational excitation spectrum (including the 1-0 S(1) line at $\lambda = 2.12\mu\text{m}$) would provide sensitivity to even hotter gas, but the mass contribution of this very hot gas in the context of our model is insubstantial.

4.1.2. Power law index, n

Keeping a fixed value of $T_u = 2000$ K, the other two model parameters, T_ℓ and n , are varied using a Levenberg-Marquardt optimization (Markwardt 2009) to match the observed line flux ratios (suitably converted to column density ratios using Eq. 11). Figure 1 is an example excitation diagram for galaxy NGC 5033. The model fit converges to $T_\ell = 51$ K, $n = 4.65$, with a fixed value of $T_u = 2000$ K. Model predicted ratio values for the unobserved lines S(4)–S(7) are indicated, as are the two discrete temperature fits chosen by Roussel et al. (2007).

The power law index n in our sample ranges from 3.79–6.39, with an average value $\bar{n} = 4.84 \pm 0.61$. Figure 2 is a frequency distribution of power law index required to fit the MIR H_2 rotational line fluxes in the SINGS galaxies. The power law index range derived in our model is comparable to the indices required to fit the H_2 rotational line fluxes for ULIRGs ($2.5 < n < 5.0$) and Seyfert galaxies (3.4–4.9) (Zakamska 2010; Pereira-Santaella et al. 2014).

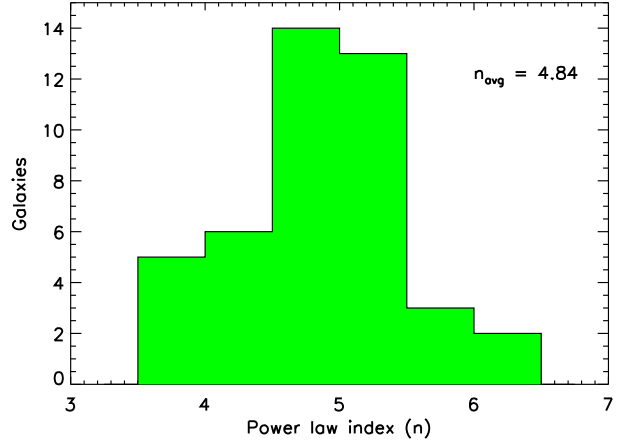


FIG. 2.— The frequency distribution of the power law index, n , required to fit the MIR H_2 rotational lines. The average value $\bar{n} = 4.84 \pm 0.61$ for the SINGS galaxy sample.

Galaxies with a steep power law index have low warm gas mass fractions, since a larger quantity of H_2 in these systems are at lower temperatures. Molecular gas heated by shocks and other turbulent energetic phenomena have higher temperatures and hence, higher warm gas mass fractions than gas in photo-dissociation regions (PDRs) (Appleton et al. in prep). The power law index therefore gives information on the relative importance of gas heating by shocks, photoelectric heating, UV pumping, etc.

4.2. Total H_2

With a continuous power law model well reproducing the rotational emission lines from warm H_2 , it is natural to consider whether the total molecular gas reservoir could be probed by suitable extrapolation of our model to lower temperatures. Typically, the entire reservoir of H_2 cannot be probed through rotational emission, since the model loses sensitivity at temperatures far below the first rotational energy state. Recovering the total molecular content from rotational H_2 emission therefore typically requires an additional free parameter — an *extrapolated* model lower temperature, T_ℓ — which must be calibrated against known molecular mass estimates. We first explore the models sensitivity to low temperatures, and then describe the calibration procedure we adopt.

4.2.1. Model Sensitivity Temperature, T_s

The upper energy level of the lowest rotational transition of H_2 is 510 K (see Table 3) — substantially higher than typical kinetic temperatures in molecular regions. Yet, even at temperatures well below this value, molecules in the high temperature tail of the energy distribution can yield detectable levels of rotational emission. Below some limiting temperature, however, increasing the number of cold H_2 molecules will increase the implied molecular gas mass, but result in no measurable changes to the H_2 rotational line fluxes.

We define the sensitivity temperature, T_s , as that temperature below which the H_2 reservoir is too cold for changes in the amount of gas to lead to measurable changes in the excitation diagram. To evaluate this in the context of our model, we calculated the difference

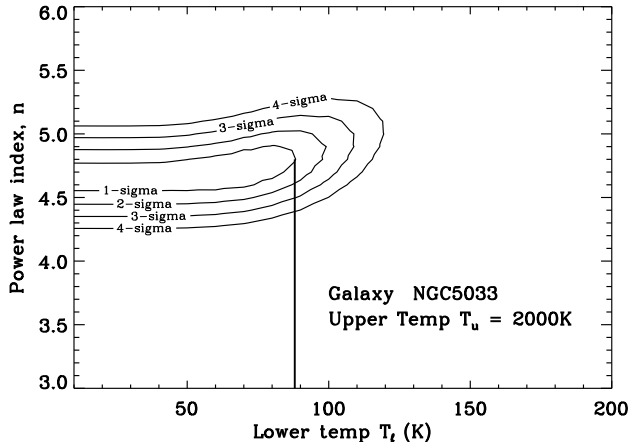


FIG. 3.— The $\Delta\chi^2$ value in the model parameter space T_ℓ and n for NGC 5033. At temperatures lower than 88 K (the maximum T_ℓ value for 1σ contour plot), the model yields similar flux ratios. Molecules with temperature less than a sensitivity temperature $T_s = 88$ K have negligible contribution to H_2 rotational line flux in the galaxy NGC 5033.

between the model-derived and observed column density ratios, $[N_u/g_u]/[(N_u/g_u)_{S(1)}]$. Note that with the adopted normalization to the $S(1)$ line, a unique excitation curve exists for any given pair n, T_ℓ ($\forall T_\ell \leq T_s$). We varied these model parameters and evaluated the quality of the model fit using

$$\chi^2 = \sum_{i=1}^m \left(\frac{R_{i,mod} - R_{i,obs}}{\sigma_{R_{i,obs}}} \right)^2, \quad (15)$$

where $R = \ln \left(\frac{N_u/g_u}{(N_u/g_u)_{S(1)}} \right)$, and $R_{i,mod}$ and $R_{i,obs}$ are, respectively, the modeled and observed flux ratios for the i^{th} transition, with uncertainty $\sigma_{R_{i,obs}}$, and the summation is over all independent line flux ratios. We map the χ^2 space in T_ℓ and n to σ values, following Avni (1976), via $\Delta\chi^2 = \chi^2 - \chi_{min}^2$ (where χ_{min}^2 is the minimum χ^2 value). Figure 3 shows example $\Delta\chi^2$ contours for the galaxy NGC 5033. The value of T_s is determined at the maximum value of lower cutoff temperature T_ℓ along the 1σ contour. For the galaxy NGC 5033, $T_s \sim 88$ K.

The near-horizontal orientation of the contours indicates little correlation between n and T_ℓ . Since for most of the sample, the contours do not close as you go towards lower temperatures $T_\ell < T_s$, any chosen lower cutoff of the power law distribution of temperatures below T_s remains consistent with the data.²

Generally, differences between the modeled and observed flux ratios decrease as T_ℓ decreases, and do not significantly change below ~ 80 K. However, in some LINER and Seyferts systems (e.g. NGC 2798, NGC 3627, and NGC 4579), the contours *close*, and χ^2 has a defined minimum. Figure 4 illustrates this phenomenon in the galaxy NGC 3627, evaluating χ^2 along the ridge line of best-fitting indices n for each T_ℓ , and contrasting this galaxy with the more typical case of an indefinite minimum. Evident in the fits to NGC 3627 is a single best-fitting lower cutoff temperature of $T_\ell \sim 120$ K. In such cases, a continuation of the power-law distribution to temperatures

² This indicates that the precise form of the temperature distribution at $T < T_s$ is not well constrained; see § 5.2.

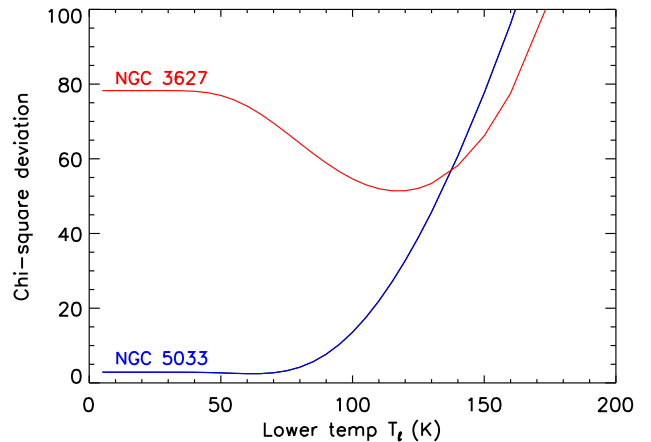


FIG. 4.— The χ^2 distribution for a normal galaxy NGC 5033 (blue) and an excess warm molecular gas galaxy NGC 3627 (red). The minimum χ^2 occurs at a cutoff temperature of 120 K for NGC 3627 however, for the galaxy NGC 5033 the χ^2 curve decreases throughout as the lower temperature is decreased. For temperatures less than 50 K the model show no change in the flux ratios since temperatures are too cold to occupy rotational energy levels and hence, a constant χ^2 curve.

below this best-fitting value is counter-indicated, as it degrades the fit. This indicates that in these cases, the bulk of H_2 is directly detected via rotational emission in a warm gas component excess.

To identify galaxies with warm molecular gas excess, we imposed the constraint $\Delta\chi^2 = \chi_{20K}^2 - \chi_{min}^2 > 2.3$, where χ_{20K}^2 is the χ^2 value at 20 K. Figures 5 and 6 show the distribution of sensitivity temperature T_s and the corresponding average confidence contour plot for all SINGS galaxies, excluding in total 8 galaxies, identified as having a warm gas excess (NGC 2798, NGC 3627, and NGC 4579) and few other galaxies (e.g. NGC 1266, NGC 1291, NGC 1316, NGC 4125, and NGC 5195) with low signal-to-noise (S/N) ratio in their $S(0)$ line. The excluded galaxies are all LINERs or Seyferts with low $S(0)/S(1)$ ratios (in the range 0.04–0.2, vs. median 0.33 in the SINGS sample, Roussel et al. (2007)). They exhibit evidence for shocks, unusually high dust temperatures, and merger morphologies — all processes that could result in substantial quantities of warm molecular gas.

As seen in Fig. 6, the average value of T_s is 81 K. This implies that, with the quality of H_2 rotational spectroscopy provided by the Spitzer/IRS instrument, H_2 gas down to rotational temperatures of ~ 80 K can be reliably detected.

4.2.2. Model extrapolated lower temperature, T_ℓ

Given our model sensitivity to H_2 columns down to rotational temperatures ~ 80 K, we evaluate the potential for *extrapolating* the power law distribution to lower temperatures to attempt to recover the the total molecular gas mass.

To calibrate an extrapolated lower temperature cutoff — T_ℓ — we require a set of galaxies with well-established molecular gas masses obtained from LCO . We constructed a training sample from SINGS galaxies (except NGC 4725, where we have an upper mass limit of molecular gas from CO intensity), omitting galaxies with a cen-

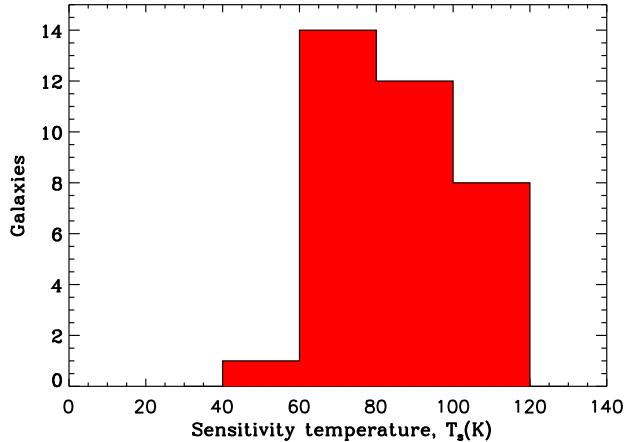


FIG. 5.— The distribution of sensitivity temperatures T_s (the temperature above which H_2 can be directly traced via rotational emission) for the SINGS sample, omitting warm excess sources. On average, the sensitivity temperature is 81 K.

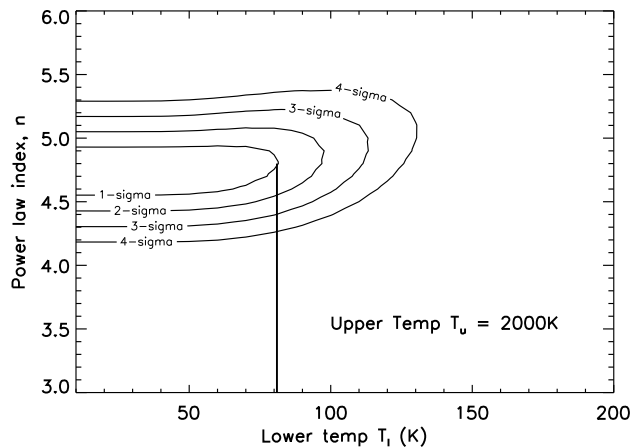


FIG. 6.— The average $\Delta\chi^2$ contours of the SINGS sample, excluding warm excess galaxies. The average value is $\overline{T_s} = 81$ K with an average power law index of $\overline{n} = 4.8$. Using these parameters, $M_{H_2}(> 81\text{K})/M_{H_2,\text{total}} = 15\%$ of the H_2 mass is probed directly via rotational emission (§ 4.2.3).

tral warm excess (see § 4.2.1). ULIRGs and radio galaxies are also avoided due to ambiguity in their α_{CO} values.

Recent studies have also shown α_{CO} in low metallicity galaxies can be substantially higher than the Galactic value (e.g. Bolatto et al. 2013; Schruba et al. 2012; Leroy et al. 2011) and hence we restricted our sample to galaxies with an oxygen abundance value of $12 + \log[\text{O}/\text{H}] \geq 8.4$, using the average of their characteristic metallicities derived from a theoretical calibration and an empirical calibration as recommended by Moustakas et al. (2010).

To perform the calibration, the single power law model fitted to the rotational excitation diagrams of each of the 34 galaxy training sample is extrapolated to the temperature where the model mass equals the cold molecular gas mass, estimated from CO emission (L_{CO}), using $\alpha_{\text{CO,Gal}}$ (column 10 of Table 2).

Figure 7 shows the distribution of extrapolated model lower temperature, T_ℓ , required to fit the molecular gas mass in the SINGS sample (with and without warm ex-

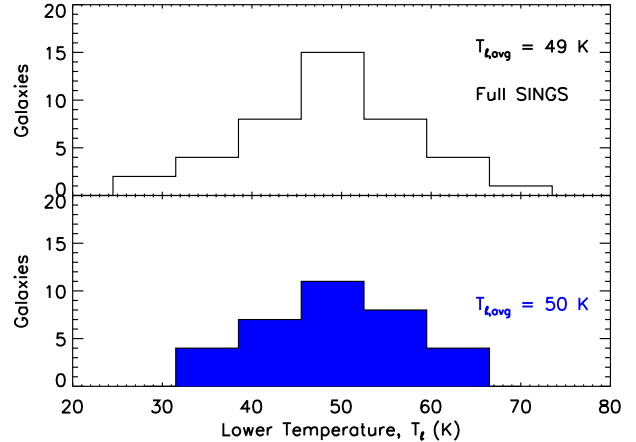


FIG. 7.— The frequency distribution of model lower temperature, T_ℓ , required to fit the molecular gas mass using the Galactic $\alpha_{\text{CO,Gal}}$. On average the value for T_ℓ is $T_\ell^* = 49$ K for our training sample. The below histogram (in blue) is plotted excluding warm galaxies with high T_s . However, no change in the average value, T_ℓ^* , is found including or excluding galaxies with warm gas excess.

cess sources). The full training sample is described by an average extrapolation temperature of $T_\ell^* = 49 \pm 9$ K. Excluding galaxies with warm gas excess narrows the distribution, but does not significantly change the average value of T_ℓ . Table 4 lists the value of T_ℓ for each galaxy, with the value in parentheses calculated when the conversion factor derived by Sandstrom et al. (2013) through dust emission is assumed.

It is important to note that the numerical value of the lower temperature cutoff of $T_\ell^* = 49 \pm 9$ K relies on the assumption of a single power law across all temperatures. See § 5.2 for an alternative viewpoint adopting broken power laws, which can change the value of T_ℓ^* without impacting the estimated total molecular gas mass.

4.2.3. Mass distribution function

Since dM/dT is a strong negative power law, the number of molecules decreases rapidly with increasing temperature — most of the H_2 gas mass resides at the lowest temperatures. We can evaluate the fraction of the total molecular mass our model is sensitive to by comparing $M(T = T_\ell \rightarrow T_s)$ and $M(T = T_s \rightarrow T_u)$

Figure 8 shows an example mass-temperature distribution dM/dT for NGC 5033 as a function of molecular temperature. The total molecular gas mass of $1.9 \times 10^8 M_\odot$ is distributed with an index $n = 4.65$ in the temperature range $T_\ell = 51$ K to $T_u = 2000$ K. The fraction of cold H_2 gas mass ($< T_s = 88$ K for NGC 5033) is $\sim 86\%$.

Using the average power-law index and sensitivity temperature from the SINGS training sample (see Fig. 6) we find $M_{H_2}(T > T_s = 81\text{K})/M_{H_2,\text{total}} \sim 15\%$. Adopting instead the 2σ contour, the value of T_s becomes 97 K and the ratio $M_{H_2}(> T_s = 97\text{K})/M_{H_2,\text{total}}$ is $\sim 8\%$. Even when considering a broken power law temperature distribution for H_2 , the mass fraction remains similar, and we discuss the effects in § 5.5. This demonstrates that, despite the many shortcomings of H_2 as a rotational emitter, *we can trace a substantial fraction of the H_2 in galaxies directly.*

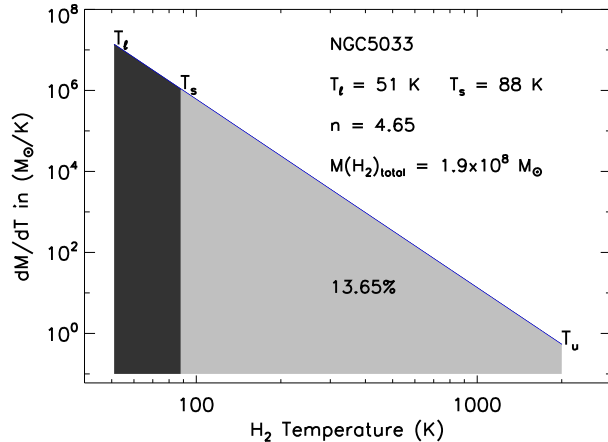


FIG. 8.— The distribution dM/dT vs molecular temperature for galaxy NGC 5033. The darker and lighter shades in the plot show two different regions, below and above the sensitivity temperature, $T_s = 88$ K. The fraction of H_2 gas mass below $T_s = 88$ K for the galaxy NGC 5033 is about 86%.

5. RESULTS, DISCUSSIONS, & APPLICATIONS

5.1. What are the typical molecular gas temperatures in galaxies?

UV pumping sets the level populations of upper level states, $J \geq 3$, in particular at low column densities of H_2 . As a result, these states may result in rotational temperatures well in excess of their kinetic temperatures. For our purposes, whatever combination of collisional (including shocks) and UV pumping determines the level populations and hence average the H_2 excitation, we assume a single power law distribution of rotational temperature describes the ensemble of molecules (although see § 5.2 for an alternative analysis employing broken power-laws). Since the mass is dominated by gas with the lowest rotational temperatures and hence lowest excitations, it is instructive to compare the derived lower temperature cutoffs (§ 4.2.2) with various theoretical models and measurements of temperature in molecular gas.

The average lower extrapolation cutoff, $T_\ell^* = 49$ K, is comparatively higher than what is typically assumed for molecular regions (~ 10 – 30 K). And yet, this high lower cutoff is essential in describing the portion of molecular material following a single power-law distribution of temperatures. For example, if we forced the extrapolation temperature to a lower value of 20 K while retaining the average power law index $n = 4.8$ (§ 4.1.2), the estimated molecular gas mass would be on average $\sim 30\times$ higher than the mass measured using L_{CO} .

The ratio of warm diffuse to cold dense molecular gas in galaxies is a key step in understanding the H_2 temperature distribution. Assuming an incident radiation field $G_0 = 10$ for a cloud with mass 10^5 – $10^6 M_\odot$, Wolfire et al. (2010) estimated that molecules in the outer diffuse region ($A_V < 1$) obtain temperatures in the range 50–80 K, with stronger incident radiation fields leading to even higher temperatures. Due to the differences in self-shielding from dissociating radiation, molecular clouds have an outer layer of varying thickness which contains molecular hydrogen, but little or no CO. This gas cannot be traced through CO transitions and is hence called

dark molecular gas (Wolfire et al. 2010). This dark gas can account for a significant fraction (24–55%) of the total molecular gas mass in galaxies (Pineda et al. 2013; Wolfire et al. 2010; Smith et al. 2014; Planck Collaboration et al. 2011).

CO-dark and diffuse molecular gas is heated to higher temperatures than dense CO-emitting gas in molecular cloud cores. Indeed, individual molecular cloud simulations find average mass-weighted H_2 temperatures of ~ 45 K for Milky-Way average cloud masses and radiation (Glover & Clark (2012a), Glover, priv. comm.). Galaxy-scale hydrodynamic simulations with a full molecular chemistry network (Smith et al. 2014) also show that H_2 gas in the CO-emitting regions is markedly biased to the low temperature end of the full temperature distribution (Glover, priv. comm.). Also, in diffuse and translucent molecular clouds in the Galaxy, Ingalls et al. (2011) demonstrated that additional sources of heating are required to explain the observed H_2 and atomic cooling-line power. Our extrapolated power law model traces both warm and cold molecular gas mass in galaxies. The common assumption that the bulk of molecular gas is found at rotational temperatures of ~ 10 – 30 K may be true only in the CO emitting core regions of the molecular cloud. The average mass-weighted molecular gas temperature can be much higher when the full range of emitting environments are considered. It is therefore perhaps not surprising to find typical molecular gas temperatures of ~ 50 K in galaxies, similar to our model derived values.

It must be noted, however, that to calculate the total molecular gas mass, we have extrapolated using a single power law index. The possibility of a broken or non-power-law temperature distribution for the $\sim 85\%$ of H_2 gas at temperatures lower than our sensitivity temperature cannot be excluded (and indeed in warm gas excess sources, will be required to explain ongoing star formation). In the following section, we consider the effect of broken power law models on the dominant H_2 temperatures.

5.2. Broken power law models

In the previous subsection we discussed the results of applying a single power law model for the entire temperature distribution of H_2 , and found that a single lower cutoff temperature of $T_\ell^* = 49$ K permits recovering the entire molecular mass. Yet as seen in § 4.2.1, with the typical performance of the Spitzer/IRS instrument, we are sensitive only to the $\sim 15\%$ of H_2 gas with temperature $T \gtrsim T_s = 81$ K. While a single power law temperature distribution, varying only the slope n , provides very high quality model fits to the H_2 excitation diagram, at temperatures below T_s , in principle *any* distribution form would provide an equally valid description. Chemo-hydrodynamic models with H_2 formation and excitation do result in a broad distribution of H_2 temperatures (Glover & Smith, in prep.). But shocks elevate H_2 to higher rotational temperatures (e.g. Neufeld & Yuan 2008), and are not well modeled, so as yet there exists no *a priori* expectation for the detailed 10–3000 K temperature distribution of H_2 molecules. Any presumed distribution, however, must 1) reproduce the H_2 excitation diagrams as well as a single power law does, and 2) permit recovering the CO-predicted H_2 mass within a reasonable range of temperatures. A *broken power-law* provides

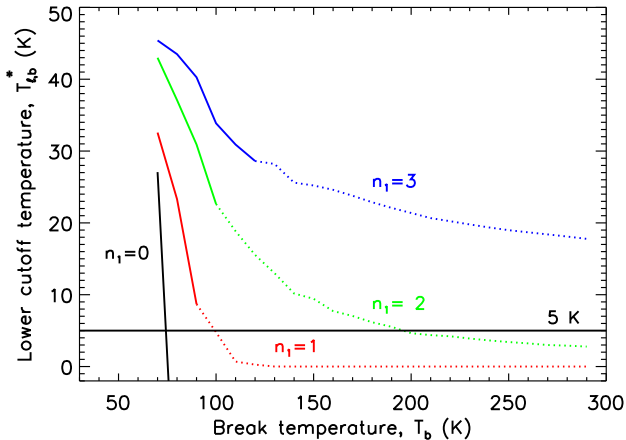


FIG. 9.— The lower extrapolation temperature for broken power-law models, $T_{\ell,b}^*$, as a function of the model break temperature, T_b for different values of lower power law indices $n_1 = 0$ (black), 1 (red), 2 (green), and 3 (blue). The solid horizontal line denotes a lower temperature physical cut off of 5 K. The dotted line in the figure shows the range where the model poorly fits the MIR H₂ rotational lines, with median $\Delta\chi^2 > 2.3$. At break temperatures above ~ 120 K, for all n_1 (0–3), the H₂ rotational lines are poorly fit.

a general framework for exploring changes in the low-temperature form of the distribution, and has been invoked by Pereira-Santaella et al. (2014) to jointly model H₂ and CO excitation. Here we consider the changes resulting from adopting a broken power law model, with a fixed break temperature, T_b , and slope below the break, n_1 , studying the resulting lower cutoff temperatures, as well as the ability of these models to satisfy these two criteria.

Holding the upper temperature T_u constant as before, we evaluated a grid of broken power law models with fixed pre-break slope n_1 (from 0–3) and break temperature T_b (from 70–290 K). For each such model, we fitted the observed MIR H₂ rotational line ratios in excitation diagrams in the same training sample of 34 galaxies considered in § 4.2.2. As before, we then extrapolate the broken power law to recover the total H₂ mass, as indicated by CO intensity, evaluating the associated extrapolation cutoff temperature $T_{\ell,b}$. We define $T_{\ell,b}^*$ as the average value of $T_{\ell,b}$ across the training sample, analogous to T_{ℓ}^* for a single power law (§ 4.2.2).

Figure 9 shows the variation of the training sample’s average extrapolated lower cutoff temperature $T_{\ell,b}^*$ as a function of break temperature T_b for differing values of below-the-break slope. Those combinations of (n_1, T_b) for which the excitation diagrams are reproduced as well as a single power law model ($\Delta\chi^2 < 2.3$ relative to the single power law model fit; see § 4.2.1) for at least 50% of the training sample are shown in solid lines. In this allowable range of n_1 and T_b , the dispersion of the ratio $M(\text{H}_2, \text{model})/M(\text{H}_2, \text{CO})$ of H₂ mass recovered from the broken power-law model using a single extrapolation $T_{\ell,b}^*$, relative to that implied by CO ranges only from 0.28–0.34 dex. At higher temperatures the excitation diagram fit quality degrades rapidly (dotted lines). As the break temperature approaches the average slope for a single power law model, $T_b = T_{\ell}^* = 49$ K, the broken power law becomes equivalent to our single power

law truncated at this temperature, independent of slope n_1 . At slopes approaching the single-power law average $n = 4.8$ (see Fig. 2), lower extrapolated temperatures diverge less and less from the value obtained using a single power law, since the shape of the temperature distribution is then relatively unchanged. Low slopes n_1 require very low extrapolation temperatures, since the cumulative mass of H₂ rises less rapidly at lower temperatures compared to the single power law. In fact, models with a flat slope ($n_1 = 0$) fail to recover the CO-derived H₂ mass within a reasonable lower H₂ temperature floor of ~ 5 K.

Figure 9 demonstrates that the single lower cutoff temperature to which an H₂ model must be extrapolated depends sensitively on the detailed shape of the distribution at low temperature. For reasonable slopes, the dominant mass-weighted temperature can range from 10–50 K. All models which produce satisfactory fits of the excitation diagrams and have physically reasonable extrapolation temperatures have nearly the same predictive capability for the total H₂ mass. While optical depth effects introduce some difficulties (e.g. for low-J ¹²CO), ideally a family of profiles for the full temperature distribution of molecular gas in galaxies could be developed, based on tracers with sensitivity to different parts of the temperature range matched to chemo-hydrodynamic models of molecular gas across all densities. Since the single power law model provides excellent fits to H₂ rotational emission line ratios with the minimum of free parameters, we retain this simplified model for the remainder of this work. It should, however, be kept in mind that broken power law models with flatter slopes below $T \sim 100$ –120 K can produce similar quality fits and yield equivalently reliable model-based H₂ masses, as long as the low temperature slope n_1 does not vary substantially from galaxy to galaxy.

5.3. Estimating total M_{H_2}

By fitting a continuous temperature distribution to the MIR H₂ rotational lines and calibrating an extrapolating temperature, this model can be used to calculate the total molecular mass in galaxies directly from H₂ rotational emission. While this method does require a reliable source of known molecular masses for calibration (introducing secondary dependence on, e.g. α_{CO}), once calibrated it is independent of any indirect tracer like CO, DGR, or assumptions about star formation depletion timescales. The biases inherent in this method (arising, for example, from the assumption of a single and smooth power law temperature distribution), are therefore expected to be relatively distinct from those of the aforementioned estimators. In this section we test the model’s capability to estimate molecular gas mass in different types of galaxies.

Adopting a fixed model lower extrapolation temperature $T_{\ell}^* = 49$ K the total H₂ gas mass is calculated by extrapolating the fitted model. The total H₂ gas mass derived by our model is shown in Figure 10. It compares very well with L_{CO} along with $\alpha_{\text{CO,Gal}}$ based estimates of gas mass. The scatter in our model is about 0.31 dex (factor of 2) for the SINGS sample and increases to 0.34 dex (factor of 2.2) for the complete sample, including U/LIRGs and radio galaxies. Some of this scatter no doubt arises from ignorance of the true α_{CO} values in

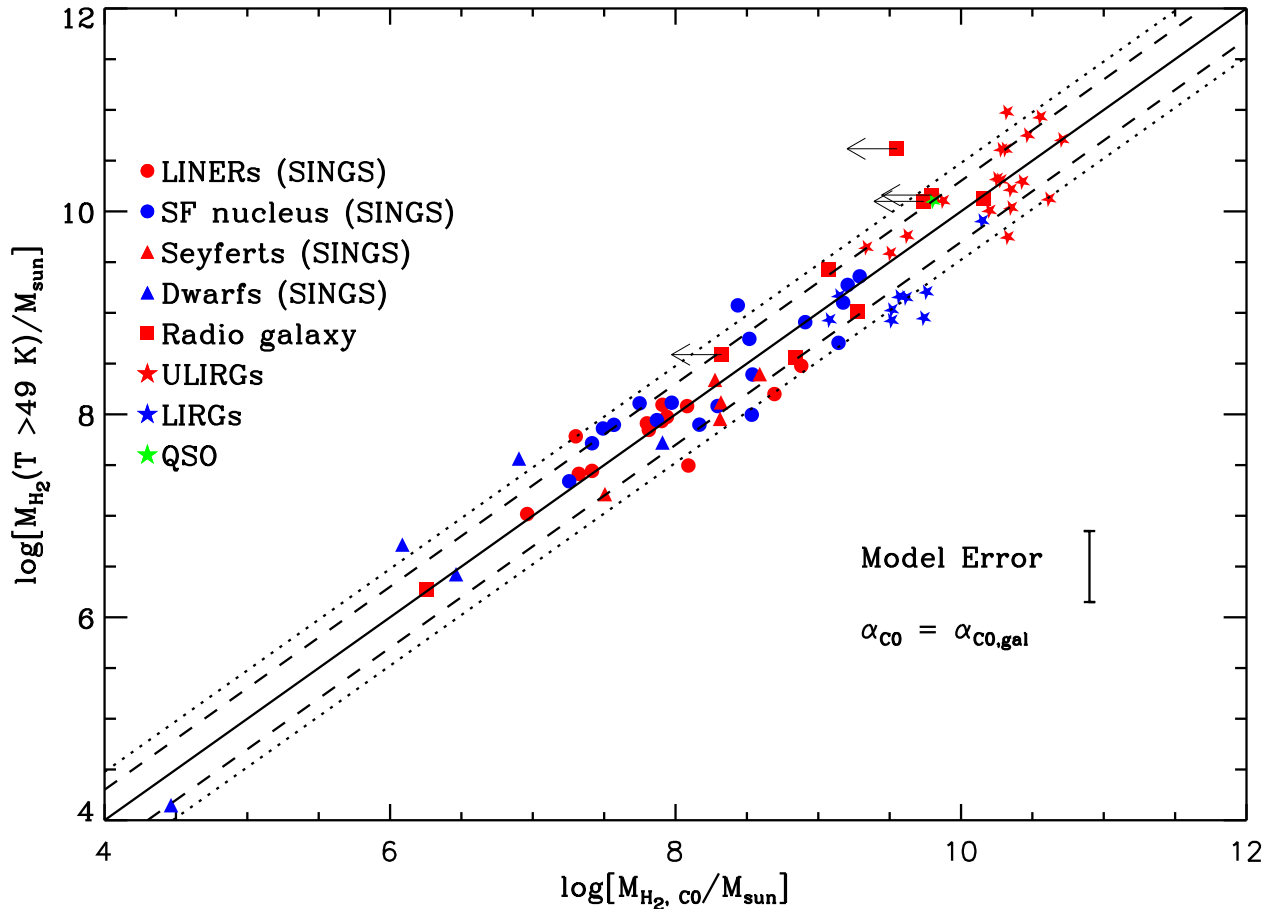


FIG. 10.— The model extrapolated molecular gas mass, assuming a single lower cutoff temperature of 49 K vs the total molecular gas mass obtained from L_{CO} measurements using $\alpha_{\text{CO,Gal}}$. Different symbols represent different galactic systems as indicated. The solid line is one to one correspondence while the dashed and dotted lines are $2\times$ and $3\times$ the value respectively.

these systems.

Galaxies with warm gas excess and a high sensitivity temperature T_s (§ 4.2.1), require similar values of extrapolated T_ℓ as the training sample. The warm molecular gas traced by MIR rotational lines may be completely isolated from the cooler gas in these galaxies. Extrapolating to a lower temperature of 49 K yields molecular gas masses which agree with CO-derived values, assuming $\alpha_{\text{CO}} = \alpha_{\text{CO,Gal}}$. A possibility of enhanced CO excitation due to high molecular gas temperature with a corresponding low α_{CO} in such warm galaxies cannot be ruled out (see also § 5.4).

Taken together, a tight correlation between H_2 -derived and CO-based mass estimates is found, spanning seven orders of magnitude in mass scale and across a wide range of galaxy types. The mass calculated with a continuous temperature distribution model, extrapolated to a single *fixed* cutoff temperature of 49 K can provide an independent measurement of total molecular gas mass in galaxies, good to within a factor of 2.2 (0.34 dex). A dependence on α_{CO} does arise indirectly through our CO-based mass estimates in the training sample (§ 4.2.2), but the recovered dispersion is comparable to uncertainties in the α_{CO} conversion factor itself, even among normal galaxies (Bolatto et al. 2013), as well as methods using DGR (e.g. Sandstrom et al. 2013).

5.4. Model derived molecular gas mass in ULIRGs, LIRGs and radio galaxies

Many local ULIRGs are recent ongoing galaxy mergers. In the merging process a large amount of gas in the spiral disk is driven to the central nuclear region, increasing the gas temperature. The increase in temperature and turbulence increases the CO linewidth, resulting in a high value of L_{CO} for a given molecular gas mass. $\alpha_{\text{CO,Gal}}$ therefore gives an overestimate of H_2 gas masses in these galaxies (Downes et al. 1993; Bryant & Scoville 1999). Moreover, $\alpha_{\text{CO,Gal}}$ can yield molecular gas masses greater than the observed dynamical mass (Solomon et al. 1997). To avoid this, a lower value of conversion factor is suggested for ULIRGs and other merger systems — $\alpha_{\text{CO}} = 0.8 M_\odot (\text{K km s}^{-1} \text{pc}^2)^{-1}$, $5.5\times$ lower than the standard Galactic value (Downes & Solomon 1998). However, by considering the high-J CO ladder, some studies have suggested that even for ULIRGs $\alpha_{\text{CO,Gal}}$ values are possible (Papadopoulos et al. 2012). Some H_2 emission may lie outside photo-dissociation and star forming regions in ULIRGs (Zakamska 2010). This H_2 may reside in CO-dark gas, so that applying a low α_{CO} value in ULIRGs may yield an underestimate H_2 mass.

In radio galaxies molecular gas can be predominantly heated by shocks through powerful jets. The molecular

gas clouds may be affected by turbulence, and not gravitationally bound, defying the use of standard $\alpha_{\text{CO,Gal}}$. Ogle et al. (2014) using DGR in NGC 4258, a low luminosity AGN (LLAGN) harboring a jet along the disk, derived gas mass of about $10^8 M_{\odot}$, an order of magnitude lower compared to the standard method of using $\alpha_{\text{CO,Gal}}$. The molecular gas mass could be overestimated when used $\alpha_{\text{CO,Gal}}$ in radio galaxies, which harbor long collimated powerful jets.

In applying a power law model to the sample of ULIRGs, LIRGs and radio galaxies, the nominal model extrapolation temperature $T_{\ell}^* = 49 \text{ K}$ is used to calculate the total H_2 gas masses, listed in column 3 of Table 5. The T_{ℓ} in column 4 of Table 5 is the required extrapolated temperature to match the cold molecular gas mass measured from the CO line intensity.

In radio galaxies 3c 424, 3c 433, cen A, and 3c 236 the estimated H_2 gas mass using the power law model after extrapolation to $T_{\ell}^* = 49 \text{ K}$, is higher when compared to the CO luminosity derived values using $\alpha_{\text{CO,Gal}}$. However, when accounted for the intrinsic variation in $\alpha_{\text{CO,Gal}}$ and T_{ℓ}^* the H_2 gas masses are in agreement with each other except in 3c 424, where the difference in masses is more than $10\times$.

Using $\alpha_{\text{CO}} = 0.8 M_{\odot}(\text{K km s}^{-1} \text{ pc}^2)^{-1}$, a factor of $5.5\times$ lower than the standard Galactic value, we derive a modified extrapolation temperature T'_{ℓ} , which is required to match the lowered gas mass. Since the model mass rises rapidly to lower temperatures, $T'_{\ell} > T_{\ell}$. The T'_{ℓ} values are listed in column 7 of Table 5. On average for ULIRGs, $T'_{\ell} = 80 \pm 13 \text{ K}$.

Figure 11 shows the temperature distribution of T_{ℓ} (adopting $\alpha_{\text{CO,Gal}}$) and T'_{ℓ} (adopting $\alpha_{\text{CO,Gal}}/5.5$) in ULIRGs. The lower temperature cutoff in ULIRGs and radio galaxies (except 3c424) is very similar to the normal galaxy training sample when $\alpha_{\text{CO,Gal}}$ is adopted, but much higher with the reduced molecular mass of $\alpha_{\text{CO,ULIRG}}$.

It is of interest that when $\alpha_{\text{CO,Gal}}$ is used with the nominal calibration cutoff temperature T_{ℓ}^* , the ULIRG sample in Fig. 10 does not exhibit any particular bias. Either α_{CO} and T_{ℓ} are similar to their normal Galactic values in these systems, or they have reduced α_{CO} and a higher H_2 temperature floor. This may indicate that the same physical processes that lead to reduced α_{CO} in highly active system, including increased ISM pressure and radiation density, globally elevate the gas temperature.

Since ULIRGs could indeed have uniformly elevated molecular gas temperatures, this degeneracy between α_{CO} decrease and T_{ℓ} increase leads to a systematic uncertainty in the total H_2 gas mass identical in form to that obtained directly from mass estimates based on L_{CO} . A suggested prescription which side-steps this ambiguity, in applying this model to systems with non-Galactic α_{CO} is to calculate the total gas mass using the the nominal $T_{\ell}^* = 49 \text{ K}$, and scale it by $\alpha_{\text{CO}}/\alpha_{\text{CO,Gal}}$, for the preferred α_{CO} . As can be seen in Fig. 10, which adopts a uniform $\alpha_{\text{CO,Gal}}$, the molecular mass in ULIRGs is well recovered by this procedure.

5.5. Effect of dust temperature on the warm H_2 fraction

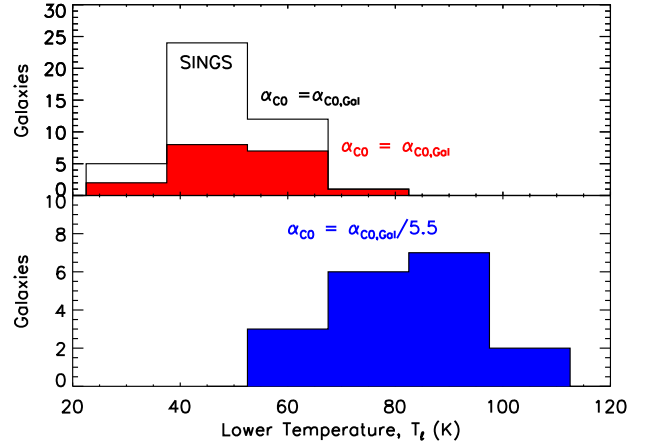


FIG. 11.— The distribution of model extrapolated lower temperatures in ULIRG and radio galaxies when the H_2 gas mass is evaluated using the Galactic conversion factor $\alpha_{\text{CO,Gal}}$ (above, red), and when adopting $\alpha_{\text{CO,Gal}}/5.5$, as generally accepted for ULIRGs (below, blue). The mean lower temperature cutoff is 50 K and 80 K when $\alpha_{\text{CO,Gal}}$ and $\alpha_{\text{CO,Gal}}/5.5$ are used, respectively. The T_{ℓ} distribution for the SINGS normal galaxy sample is shown above, for comparison.

Since typical sensitivity temperatures are $T_s \sim 80 \text{ K}$ (see § 4.2.1), we can directly calculate the warm H_2 mass above $\sim 100 \text{ K}$ without extrapolation, and compare it to the total mass as recovered by the calibrated extrapolation of § 4.2.2. Given an estimate for the power law index, n , and lower cut off temperature, T_{ℓ} , of the power law distribution, we can calculate the fraction of molecular gas mass at temperatures above 100 K as

$$\frac{M(> 100 \text{ K})}{M_{\text{total}}} = \frac{M(> 100 \text{ K})}{M(\text{H}_2, \text{CO})} = \frac{\int_{100\text{K}}^{T_u} T^{-n} dT}{\int_{T_{\ell}}^{T_u} T^{-n} dT}, \quad (16)$$

where M_{total} is the total molecular gas mass estimated from the CO line intensity. Assuming $100 \text{ K} \ll T_u$ and $T_{\ell} \ll T_u$ we find

$$\frac{M(> 100 \text{ K})}{M_{\text{total}}} \approx \left(\frac{100 \text{ K}}{T_{\ell}} \right)^{1-n}. \quad (17)$$

Table 4 lists the calculated mass fraction $M(> 100\text{K})/M_{\text{total}}$ for each galaxy. Columns 6 and 8 of Table 5 are calculated using $\alpha_{\text{CO,Gal}}$ and $(1/5.5) \times \alpha_{\text{CO,Gal}}$ as generally assumed for ULIRGs, respectively. At lower α_{CO} , the warm gas mass fraction is higher.

Figure 12 shows the fraction of warm molecular gas mass, $M(> 100\text{K})/M_{\text{total}}$, as a function of far infrared (FIR) dust color temperature, $\nu_{70\mu\text{m}}/\nu_{160\mu\text{m}}$. The warm gas fraction obtained using $\alpha_{\text{CO,Gal}}$ ranges from 2–30%, and exhibits little correlation among different galaxy types with dust color temperature. The ULIRGs and normal star forming galaxies show similar warm gas fractions, though ULIRGs have warmer dust color temperatures, and LINERs and Seyferts have somewhat higher warm gas mass fractions than normal star forming galaxies on average.

In contrast, using the available dust-derived central α_{CO} estimates of Sandstrom et al. (2013) for normal galaxies and a reduced value $\frac{1}{5.5} \times \alpha_{\text{CO,Gal}}$ for ULIRGs and QSO's, however, leads to a strong correlation, with

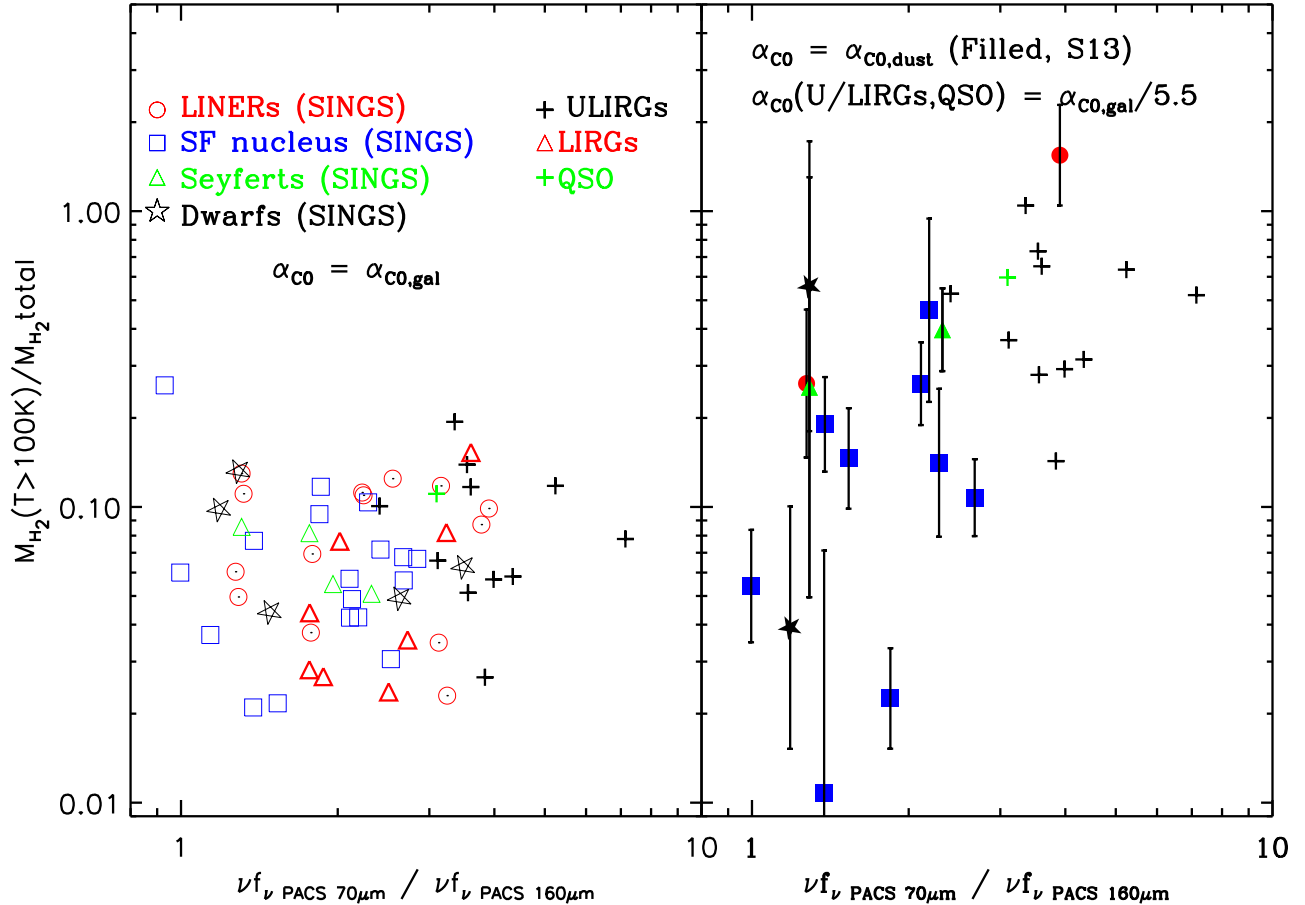


FIG. 12.— The fraction of warm H_2 gas mass ($T > 100\text{ K}$) versus the dust color temperature, $\nu f_{\nu, 70\mu\text{m}} / \nu f_{\nu, 160\mu\text{m}}$, obtained from PACS. At left a consistent Galactic α_{CO} is adopted, and little trend is seen. At right, a reduced α_{CO} is applied to ULIRGs and QSO, and the dust-derived central α_{CO} values of Sandstrom et al. (2013) are used. Galaxies with warmer dust color temperatures have high warm molecular gas mass fraction.

warmer dust implying an increasing warm H_2 fraction. The average warm gas fraction for ULIRGs and QSO is then $\sim 45\%$, significantly above that of normal galaxies, and on the same increasing trend with dust temperature. Depending on which prescription for total gas mass is correct, this could indicate a dependence of α_{CO} on temperature.

When considering a broken power law model, the fraction $M(>100\text{ K})/M_{\text{total}}$ is, as expected, very similar to that of a single power law for $T_b \leq 100\text{ K}$. For $T_b > 120\text{ K}$ irrespective of low-temperature slope n_1 , the model yields a poor fit to the excitation diagrams (see § 5.2). At these intermediate break temperatures, the warm mass fraction $M(>100\text{ K})/M_{\text{total}}$ changes by at most $\sim 10\text{--}20\%$ compared to the case of a single power law.

5.6. Molecular gas in low metallicity galaxies

As traced by their CO emission, many low metallicity dwarfs appear to have vanishingly low molecular gas content, but retain high star formation rates. That is, they are strong outliers on the Schmidt-Kennicutt relation (Galametz et al. 2009; Schruba et al. 2012). This discrepancy implies either that in dwarf galaxies star formation efficiencies are higher compared to normal spi-

als, or they host large molecular gas reservoirs than is traced by the CO emission (Schruba et al. 2012; Glover & Clark 2012b). It is possible that a significant fraction of H_2 exists outside the CO region, where the carbon is in C^+ (ionized) or C^0 (neutral) states. Since H_2 can self-shield from UV photons in regions where CO is photodissociated (Wolfire et al. 2010), at low metallicity, not only is the CO abundance reduced, but as dust opacity is reduced and ionized regions become hotter and more porous, $\alpha_{\text{CO,Gal}}$ can severely underestimate the molecular gas mass. Considerable effort has been invested in detecting and interpreting CO emission at metallicity 50 times lower than the solar metallicity, $12 + \log[\text{O}/\text{H}] \sim 7.0$, to assess the molecular gas content (Leroy et al. 2011; Schruba et al. 2012; Cormier et al. 2014; Rémy-Ruyer et al. 2014). Dust emission can be used to estimate the molecular gas mass in ISM, assuming a constant DGR however, it is essential to know the change in DGR with metallicity. At very low metallicities, $12 + \log[\text{O}/\text{H}] \leq 8$, DGR appears to scale non-linearly with metallicity (Herrera-Camus et al. 2012; Rémy-Ruyer et al. 2014).

Our direct detection of H_2 gas mass through H_2 rotational lines is independent of any indirect tracers, which are affected by changing metallicity and local radiation

effects. Applying our model in low metallicity galaxies should yield an estimate of molecular gas mass without the same inherent biases introduced by these dust and CO abundance variations. In this section we estimate the H₂ gas masses through our power law model in a low metallicity galaxy sample selected to have detected H₂ rotational emission, faint CO detection, and (where available) estimates of dust mass. We then compare these H₂-based estimates to models and other methods which attempt to control for the biases introduced at low metallicity.

The low metallicity galaxies were selected on availability of MIR H₂ rotational lines to have at least three rotational lines including S(0) or S(1) line fluxes along with CO derived molecular mass estimates.

5.6.1. Metallicity estimation

To study the variation of H₂ gas mass from CO derived measurements over the metallicity range, it is essential to estimate the metallicity of galaxies. The metallicities were determined applying the direct T_e method. CGCG 007-025 is the lowest metallicity galaxy in our dwarf sample with the value of $12 + \log[\text{O}/\text{H}] = 7.77$ (Izotov et al. 2007). Guseva et al. (2012) estimated the value of $12 + \log[\text{O}/\text{H}]$ in the two H II regions, Haro 11B and Haro 11C as 8.1 and 8.33, respectively hence, we adopt the average value for Haro 11. The metallicity value, $12 + \log[\text{O}/\text{H}]$, for NGC 6822 is 8.2 (Israel 1997). No literature value exist for the oxygen gas phase abundance for the specific region of Hubble V in NGC 6822, mapped by the IRS-Spitzer. Peimbert et al. (2005) estimated $12 + \log[\text{O}/\text{H}] = 8.42 \pm 0.06$ for Hubble V, which is inconsistent with the previous value of 8.2.

For selected SINGS galaxies, the metallicity values in the circumnuclear regions, which are approximately the size of our H₂ line flux extracted regions, are estimated by averaging the theoretical (KK04) and an empirical metallicity calibration (PTO5) as recommended by Moustakas et al. (2010).

5.6.2. Cold molecular gas from CO line emission

Although the CO abundance drops super-linearly with decreasing metallicity, it is detected in the low metallicity sample, and as the most common molecular tracer, can be compared directly to our H₂ based method. We adopted the literature values for ¹²CO(1–0) line intensities for CGCG 007-025 and N66, while for Haro 11, UM 311 and Hubble V region ¹²CO(3–2) line intensities were scaled using the relation $I_{\text{CO}(3-2)}/I_{\text{CO}(1-0)} = 0.60$ (in temperature units) due to unavailability of ¹²CO(1–0) line intensities. Calculating L'_{CO} , (area integrated luminosity) the molecular gas masses are estimated using $\alpha_{\text{CO,Gal}}$ and were further scaled using the 8 μm map, to account for the difference in the extracted IRS spectrum and the CO beam regions for each galaxy. The molecular gas masses are listed in Table 6.

5.6.3. Molecular gas from dust emission

An alternative method for estimating molecular gas mass makes use of dust emission together with assumption of dust opacity and grain size distribution to calculate a total mass, scaling dust mass to the total gas mass using a presumed or modeled dust-to-gas ratio, and removing the measured atomic mass from the region.

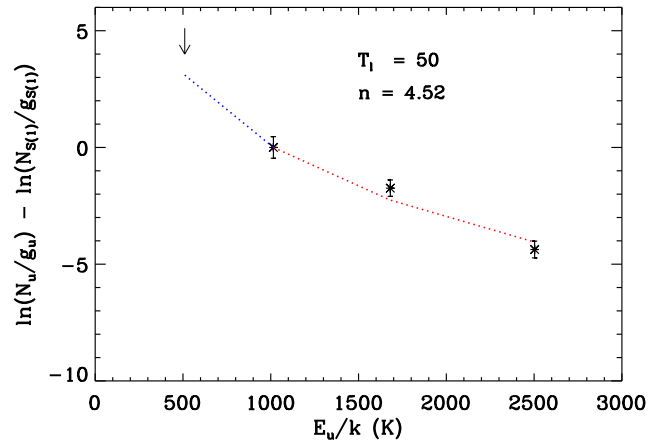


FIG. 13.— Excitation diagram for low metallicity galaxy Haro 11. The N_u/g_u ratios are normalized with respect to S(1) transition. The dashed red line indicate the model fit to the observed ratios. The blue dashed line predicts the value of S(0) flux ratio. The model estimated T_ℓ , and n are mentioned.

Leroy et al. (2007) estimated H₂ gas surface density using dust emission from FIR map in N66 region of SMC. They derived α_{CO} to be about $27 \times \alpha_{\text{CO,Gal}}$. For Haro 11, UM 311 and Hubble V using metallicity-DGR relation from Sandstrom et al. (2013) and with the known dust mass, we estimated the total gas mass and after subtracting the atomic gas content subsequently calculated the molecular gas mass. However, we find a negative value for the molecular gas for UM311, suggesting the ISM mass is mainly dominated by the atomic gas. The H₂ gas masses calculated from the dust emission are given in Table 6.

5.6.4. Molecular gas mass using our model

The H₂ line flux extraction was performed for the similar region in SMC-N66, where the CO emission was measured by Rubio et al. (1996). The cubes were prepared using CUBISM (Smith et al. 2007b) (Jameson, K. et al. in prep) and the H₂ line fluxes were estimated using the PAHFIT, a MIR spectral decomposition tool (Smith et al. 2007a). The flux of H₂ rotational lines for Haro 11 are from Cormier et al. (2014), while for UM 311, and CGCG 007-025 Hunt et al. (2010) measured the H₂ rotational line fluxes. For Hubble V region, Roussel et al. (2007) derived the flux of H₂ rotational lines.

Figure 13 is an excitation diagram for low metallicity galaxy Haro 11, with the power law model fit. Our model prediction for the unobserved S(0) line is included, and is consistent with the estimated upper limit. The H₂ total gas mass for each low metallicity galaxy is measured using the power law model with lower temperature extrapolation to $T_\ell^* = 49$ K. Table 6 lists the value of metallicity with their distance and the measured value of H₂ rotational line fluxes with the power law index and the H₂ gas mass derived using CO, dust, and our model.

Figure 14 compiles H₂ gas masses derived using the various indirect tracers, together with the results from our H₂-only model. All values are shown *relative* to the H₂ mass inferred using CO luminosities with $\alpha_{\text{CO}} = \alpha_{\text{CO,Gal}}$, and are plotted as a function of metallicity. For the SINGS sample, a variation of about 2–3

times the L_{CO} -derived H_2 gas mass is found, likely a consequence of the intrinsic variation in α_{CO} at high metallicity $12 + \log[\text{O}/\text{H}] \gtrsim 8.4$. At intermediate metallicity, the molecular gas content from CO line emission for the Hubble V region in NGC 6822 compares well with our model-derived gas mass, which suggests a similar Galactic conversion factor ($\alpha_{\text{CO}} = \alpha_{\text{CO,Gal}}$), consistent with the results of de Rijcke et al. (2006). At lower metallicity, however, our model disagrees strongly with naive CO-based estimates, yielding up to $\sim 100\times$ the molecular gas mass inferred from CO emission.

The molecular masses we recover at low metallicity are in good agreement with other measures which attempt to account for the impact of reduced metal abundance. These include dust-derived measurements, where available (when the strong metallicity dependence of the dust-to-gas ratio is accounted for). They also agree well with the prescription for the power-law like α_{CO} variations with metallicity recovered from inverting star formation densities among all non-starburst galaxies in the HERACLES sample (Schruba et al. 2012). The theoretical model of varying α_{CO} by Wolfire et al. (2010), assuming H_2 column density of 10^{22} cm^{-2} in a molecular cloud, agrees well with observational results based on dust-mass at low metallicity (Leroy et al. 2011; Sandstrom et al. 2013). Adopting a solar metallicity value of 8.66 and heating rate/H atom $\log(G_0/n) = -0.3$ (from the $L_{\text{OI}}/L_{\text{FIR}}$ studies of Malhotra et al. (2001)), the Wolfire et al. (2010) model also agrees well with our H_2 rotational emission modeled masses.

The power law model reliably recovers the total molecular gas masses at metallicity as low as 10% of the Milky Way, where CO and other indirect tracers suffer strong and non linear biases.

5.7. Future prospects

At metallicities $\lesssim 0.25 Z_{\odot}$, the direct power-law method recovers total molecular gas content as reliably as other tracers that account for or avoid the impact of reduced gas-phase metal content. At even lower metallicities, the CO abundance plummets, with essentially all of the molecular gas in a CO-dark phase. In the first epoch of the star formation in the universe, the extremely low abundance of heavy elements leaves H_2 as a principal coolant (Lepp et al. 2002).

The Mid Infrared Instrument (MIRI) onboard *JWST* is sensitive enough to detect the S(1), S(2), S(3) and higher rotational lines of H_2 in luminous galaxies (U/LIRGs) till redshift 0.6, 1.3, 1.9, and higher, respectively. Assuming average $L_{\text{H}_2\text{S}(1)}/L_{\text{IR}} = 10^{-4}$ (Bonato et al. 2015), and $L_{\text{IR}} = 3 \times 10^{11} L_{\odot}$ (typical for LIRGs), for S(1) at $z = 0.5$ to have signal to noise $S/N = 5$ will require 30 minutes of integration time with *JWST*-MIRI. It will be possible to measure pure H_2 rotational lines at high redshifts of $z \approx 6-7$, almost reaching the reionization era of universe, with the SPace Infrared telescope for Cosmology and Astrophysics (SPICA) and the Cryogenic Aperture Large Infrared Submillimeter Telescope Observatory (CALISTO), planned for the 2020 decade (Roelfsema et al. 2012; Bradford et al. 2015).

The above mentioned future projects for the next decade provides an opportunity to observe H_2 rotational lines at high redshifts. The power law model can be an useful tool in estimating molecular gas mass and study

its variation and consequences at different redshifts.

6. SUMMARY

We present a new power law temperature distribution model capable of reliably estimating the total molecular gas mass in galaxies purely from as few as three mid-infrared pure-rotational H_2 emission lines. Our model is independent of the biases affecting indirect tracers like CO, dust emission, or star formation prescriptions. It can hence be used even in environments where reliability of those indirect tracers is poor, such as at low metallicity. We calibrate the model on a sample of local star-forming galaxies with well-quantified CO-based molecular gas masses, and apply the model to local ULIRGs and low metallicity systems. Our key results are:

1. A model based on a continuous power law distribution of rotational temperatures reproduces well the H_2 excitation from a wide range of galaxy types using only a single parameter (the power law slope n). This simple model can directly recover the warm H_2 mass ($T \gtrsim 100 \text{ K}$) more reproducibly than arbitrary discrete temperature fits.
2. The power law index obtained for all SINGS galaxies ranges from 3.79 - 6.4, with an average value of 4.84 ± 0.61 .
3. With typical Spitzer detection sensitivities, the model can directly recover the H_2 gas mass down to a limiting sensitivity temperature of $T_s = 81 \text{ K}$ (when the S(0) line is available), accounting for $\sim 15\%$ of the total molecular reservoir.
4. By calibrating the model using a subset of the SINGS sample with well determined CO-based molecular masses, we find that extrapolating the H_2 temperature distribution to a *single* cutoff temperature of $T_{\ell}^* = 49 \text{ K}$ enables recovery of the total H_2 gas mass within a factor of 2.2 (0.34 dex).
5. Evaluating a family of broken power law models, we find that the average lower cutoff temperature $T_{\ell,b}^*$ could range from 5–50 K, while recovering total H_2 gas masses as well as a single power law model. However, low model slopes below the break (n_1) would require unphysically low cutoff temperatures, and for all power law indices $n_1 \leq 3$, break temperatures $T_b \gtrsim 120 \text{ K}$ result in unacceptable fits to the H_2 MIR rotational lines.
6. When $\alpha_{\text{CO,Gal}}$ is used, the fraction of warm molecular gas mass ($M > 100 \text{ K}$) in this training sample ranges from 0.02 to 0.30. If a reduced α_{CO} is adopted for the ULIRGs, this fraction increases with increasing dust color temperature $\nu f_{\nu 70 \mu\text{m}}/\nu f_{\nu 160 \mu\text{m}}$.
7. In ULIRGs, the total molecular gas mass obtained by extrapolating the model to $T_{\ell}^* = 49 \text{ K}$ is consistent with the molecular gas mass derived using $\alpha_{\text{CO,Gal}}$. Alternatively, if a reduced α_{CO} is adopted, the model extrapolation temperature required rises to 80 K. Either the warm molecular gas fraction and lower temperature cutoff in ULIRGs

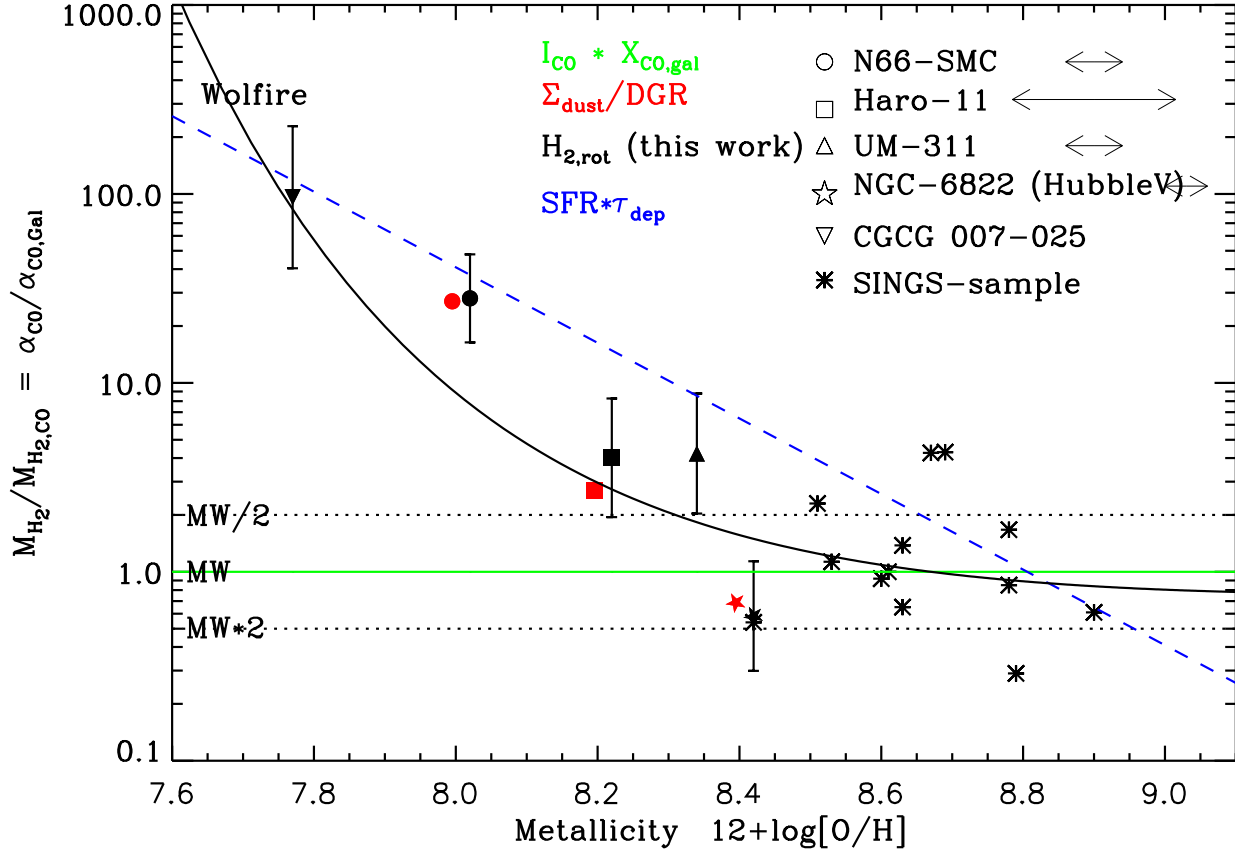


FIG. 14.— The ratio of molecular gas masses estimated using different methods to the “naive mass” obtained using L_{CO} (and $\alpha_{\text{CO}} = \alpha_{\text{CO,Gal}}$), as a function of gas-phase metallicity. This ratio is equivalent to $\alpha_{\text{CO}}/\alpha_{\text{CO,Gal}}$. The black points show the molecular gas masses derived from the H_2 rotational model. The blue line shows a fit to this ratio derived from inverting the star formation law for HERACLES non-starburst galaxies (Schruba et al. 2012). The molecular gas masses traced by the dust emission are denoted by the red points in the plot, and are shifted slightly in their metallicity values for clarity. The black solid line is the predicted mass ratio from the theoretical model of Wolfire et al. (2010), assuming $N(\text{H}_2) = 10^{22} \text{ cm}^{-2}$ and $\log(G_0/n) = -0.3$. A steep increase in the ratio of model derived H_2 gas mass to the L_{CO} derived measurements is observed at metallicity values $12 + \log[\text{O}/\text{H}] \lesssim 8.4$.

is higher than in normal star forming galaxies, or α_{CO} is closer to the Galactic value than has been presumed.

8. At low metallicity ($12 + \log[\text{O}/\text{H}] \lesssim 8.4$), where indirect tracers of molecular mass suffer increasingly strong and non-linear biases and the mass of the molecular reservoirs exceed their CO-derived estimates by $100\times$ or more, the direct power law model recovers the total molecular gas masses reliably, as assessed by other methods which account for metallicity.
9. With upcoming facilities including *JWST*, *SPICA*, and *CALISTO*, detection of the relevant H_2 rotational lines in galaxies at intermediate to high redshifts becomes possible, opening a new window on the fueling history of star formation in the Universe.

Acknowledgements: This paper is dedicated to James R. Houck of Cornell University (1940-2015), the PI of the *Spitzer IRS*. This work is based on observations made

with the *Spitzer Space Telescope*. We have made use of the NASA/IPAC Extragalactic Database (NED) which is operated by the Jet Propulsion Laboratory, California Institute of Technology under NASA contract. Support for this research was provided by NASA through contract 1287374 issued by JPL/Caltech under contract 1407. We thank the anonymous referee for useful comments and suggestions. We are grateful to K. Jameson and A. Bolatto for sharing the N66-SMC region spectrum. We are also indebted to L. Armus, N. Scoville, B. Draine, A. Bolatto, S. R. Federman, K. Sandstrom, D. Neufeld, F. Walter, T. Diaz-Santos, E. Pellegrini for discussions which improved this work, and to S. Glover for providing model access and for helpful discussions of simulated H_2 temperature in galaxies. JDS gratefully acknowledges visiting support from the Alexander von Humboldt Foundation and the Max Planck Institute für Astronomie, and support from a Cottrell Scholar Award from the Research Corporation for Science Advancement. AT acknowledges support for this work through the IPAC Visiting Graduate Fellowship program.

REFERENCES

- Appleton, P. N., Xu, K. C., Reach, W., et al. 2006, *ApJ*, 639, L51
- Armus, L., Bernard-Salas, J., Spoon, H. W. W., et al. 2006, *ApJ*, 640, 204
- Avni, Y. 1976, *ApJ*, 210, 642
- Bhat, C. L., Issa, M. R., Houston, B. P., Mayer, C. J., & Wolfendale, A. W. 1985, *Nature*, 314, 511
- Black, J. H., & Dalgarno, A. 1976, *ApJ*, 203, 132
- Bloemen, J. B. G. M., Caraveo, P. A., Hermsen, W., et al. 1984, *A&A*, 139, 37
- Bloemen, J. B. G. M., Strong, A. W., Mayer-Hasselwander, H. A., et al. 1986, *A&A*, 154, 25
- Bigiel, F., Leroy, A., Walter, F., et al. 2008, *AJ*, 136, 2846
- Bolatto, A. D., Wolfire, M., & Leroy, A. K. 2013, *ARA&A*, 51, 207
- Bonato, M., Negrello, M., Cai, Z.-Y., et al. 2015, *MNRAS*, 452, 356
- Bradford, C. M., Goldsmith, P. F., Bolatto, A., et al. 2015, *arXiv:1505.05551*
- Browning, M. K., Tumlinson, J., & Shull, J. M. 2003, *ApJ*, 582, 810
- Bryant, P. M., & Scoville, N. Z. 1999, *AJ*, 117, 2632
- Burton, M. G., Hollenbach, D. J., & Tielens, A. G. G. M. 1992, *ApJ*, 399, 563
- Burton, M. G. 1987, Ph.D. Thesis
- Cormier, D., Madden, S. C., Lebouteiller, V., et al. 2014, *A&A*, 564, A121
- Curran, S. J., Aalto, S., & Booth, R. S. 2000, *A&AS*, 141, 193
- Dabrowski, I. 1984, *Canadian Journal of Physics*, 62, 1639
- de Rijcke, S., Buyle, P., Cannon, J., et al. 2006, *A&A*, 454, L111
- van Dishoeck, E. F., & Black, J. H. 1986, *Interstellar Processes: Abstracts of Contributed Papers*, 149
- Downes, D., Solomon, P. M., & Radford, S. J. E. 1993, *ApJ*, 414, L13
- Downes, D., & Solomon, P. M. 1998, *ApJ*, 507, 615
- Draine, B. T., & McKee, C. F. 1993, *ARA&A*, 31, 373
- Draine, B. T. 2011, *Physics of the Interstellar and Intergalactic Medium* by Bruce T. Draine. Princeton University Press, 2011. ISBN: 978-0-691-12214-4.
- Draine, B. T., Dale, D. A., Bendo, G., et al. 2007, *ApJ*, 663, 866
- Dufour, R. J. 1984, *Structure and Evolution of the Magellanic Clouds*, 108, 353
- Dufour, R. J., Shields, G. A., & Talbot, R. J., Jr. 1982, *ApJ*, 252, 461
- Egami, E., Rieke, G. H., Fadda, D., & Hines, D. C. 2006, *ApJ*, 652, L21
- Evans, A. S., Sanders, D. B., Surace, J. A., & Mazzarella, J. M. 1999, *ApJ*, 511, 730
- Evans, A. S., Frayer, D. T., Surace, J. A., & Sanders, D. B. 2001, *AJ*, 121, 1893
- Evans, A. S., Mazzarella, J. M., Surace, J. A., & Sanders, D. B. 2002, *ApJ*, 580, 749
- Evans, A. S., Mazzarella, J. M., Surace, J. A., et al. 2005, *ApJS*, 159, 197
- Field, G. B., Somerville, W. B., & Dressler, K. 1966, *ARA&A*, 4, 207
- Fisher, D. B., Bolatto, A. D., Herrera-Camus, R., et al. 2014, *Nature*, 505, 186
- Galametz, M., Madden, S., Galliano, F., et al. 2009, *A&A*, 508, 645
- Galliano, F., Madden, S. C., Jones, A. P., et al. 2003, *A&A*, 407, 159
- Genzel, R., Tacconi, L. J., Combes, F., et al. 2012, *ApJ*, 746, 69
- Genzel, R., Tacconi, L. J., Lutz, D., et al. 2015, *ApJ*, 800, 20
- Glover, S. C. O., & Clark, P. C. 2012a, *MNRAS*, 421, 9
- Glover, S. C. O., & Clark, P. C. 2012b, *MNRAS*, 426, 377
- Guillard, P., Ogle, P. M., Emonts, B. H. C., et al. 2012, *ApJ*, 747, 95
- Guseva, N. G., Izotov, Y. I., Fricke, K. J., & Henkel, C. 2012, *A&A*, 541, A115
- Hanel, R., Conrath, B., Flasar, M., et al. 1979, *Science*, 206, 952
- Hanel, R., Conrath, B., Flasar, F. M., et al. 1981, *Science*, 212, 192
- Harnett, J. I., Wielebinski, R., Bajaja, E., Reuter, H.-P., & Hummel, E. 1991, *Proceedings of the Astronomical Society of Australia*, 9, 258
- Herrera-Camus, R., Fisher, D. B., Bolatto, A. D., et al. 2012, *ApJ*, 752, 112
- Higdon, S. J. U., Armus, L., Higdon, J. L., Soifer, B. T., & Spoon, H. W. W. 2006, *ApJ*, 648, 323
- Houck, J. R., Roellig, T. L., van Cleve, J., et al. 2004, *ApJS*, 154, 18
- Hollenbach, D. J., & Tielens, A. G. G. M. 1999, *Reviews of Modern Physics*, 71, 173
- Hollenbach, D. J., & Tielens, A. G. G. M. 1997, *ARA&A*, 35, 179
- Hollenbach, D., & McKee, C. F. 1979, *ApJS*, 41, 555
- Huber, K. P., & Herzberg, G. 1979, *Constants of Diatomic Molecules* (New York: Van Nostrand)
- Hudson, R. D. 1971, *Reviews of Geophysics and Space Physics*, 9, 305
- Hunt, L. K., Thuan, T. X., Izotov, Y. I., & Sauvage, M. 2010, *ApJ*, 712, 164
- Hunt, L. K., García-Burillo, S., Casasola, V., et al. 2015, *A&A*, 583, A114
- Ingalls, J. G., Bania, T. M., Boulanger, F., et al. 2011, *ApJ*, 743, 174
- Israel, F. P., Bontekoe, T. R., & Kester, D. J. M. 1996, *A&A*, 308, 723
- Israel, F. P. 1997, *A&A*, 328, 471
- Israel, F. P., van Dishoeck, E. F., Baas, F., et al. 1990, *A&A*, 227, 342
- Israel, F. P., Baas, F., Rudy, R. J., Skillman, E. D., & Woodward, C. E. 2003, *A&A*, 397, 87
- Izotov, Y. I., & Thuan, T. X. 1998, *ApJ*, 500, 188
- Izotov, Y. I., Thuan, T. X., & Stasińska, G. 2007, *ApJ*, 662, 15
- Kennicutt, R. C., Jr. 1998, *ApJ*, 498, 541
- Kennicutt, R. C., Jr., Armus, L., Bendo, G., et al. 2003, *PASP*, 115, 928
- Lavezzi, T. E., & Dickey, J. M. 1998, *AJ*, 115, 405
- Lepp, S., Stancil, P. C., & Dalgarno, A. 2002, *Journal of Physics B Atomic Molecular Physics*, 35, 57
- Leroy, A., Bolatto, A., Stanimirovic, S., et al. 2007, *ApJ*, 658, 1027
- Leroy, A. K., Bolatto, A., Gordon, K., et al. 2011, *ApJ*, 737, 12
- Lutz, D., Sturm, E., Genzel, R., et al. 2003, *A&A*, 409, 867
- Malhotra, S., Kaufman, M. J., Hollenbach, D., et al. 2001, *ApJ*, 561, 766
- Markwardt, C. B. 2009, *Astronomical Data Analysis Software and Systems XVIII*, 411, 251
- Mirabel, I. F.; Sanders, D. B. & Kazes, I. 1989, *ApJ*, 340, L9
- Moustakas, J., Kennicutt, R. C., Jr., Tremonti, C. A., et al. 2010, *ApJS*, 190, 233
- Nesvadba, N. P. H., Boulanger, F., Salomé, P., et al. 2010, *A&A*, 521, A65
- Neufeld, D. A., & Yuan, Y. 2008, *ApJ*, 678, 974
- Ocaña Flaquer, B., Leon, S., Combes, F., & Lim, J. 2010, *A&A*, 518, A9
- O'Dowd, M. J., Schiminovich, D., Johnson, B. D., et al. 2009, *ApJ*, 705, 885
- Ogle, P., Boulanger, F., Guillard, P., et al. 2010, *ApJ*, 724, 1193
- Ogle, P., Davies, J. E., Appleton, P. N., et al. 2012, *ApJ*, 751, 13
- Ogle, P. M., Lanz, L., & Appleton, P. N. 2014, *ApJ*, 788, L33
- Okuda, T., Kohno, K., Iguchi, S., & Nakanishi, K. 2005, *ApJ*, 620, 673
- Pereira-Santaella, M., Alonso-Herrero, A., Rieke, G. H., et al. 2010, *ApJS*, 188, 447
- Pereira-Santaella, M., Spinoglio, L., van der Werf, P. P., & Piqueras López, J. 2014, *A&A*, 566, A49
- Padelis P. Papadopoulos, Paul van der Werf; Xilouris, E.; Isaak, K. G. & Yu Gao 2012, *ApJ*, 751, 10
- Peimbert, A., Peimbert, M., & Ruiz, M. T. 2005, *ApJ*, 634, 1056
- Pineda, J. L., Langer, W. D., Velusamy, T., & Goldsmith, P. F. 2013, *A&A*, 554, A103
- Planck Collaboration, Ade, P. A. R., Aghanim, N., et al. 2011, *A&A*, 536, AA19
- Poglitsch, A., Waelkens, C., Geis, N., et al. 2010, *A&A*, 518, L2
- Rachford, B. L., Snow, T. P., Tumlinson, J., et al. 2002, *ApJ*, 577, 221
- Rémy-Ruyer, A., Madden, S. C., Galliano, F., et al. 2014, *A&A*, 563, A31
- Rigopoulou, D.; Lawrence, A.; White, G. J., Rowan Robinson, M., & Church, S. E. 1996, *A&A*, 305, 747
- Roelfsema, P., Giard, M., Najarro, F., et al. 2012, *Proc. SPIE*, 8442, 84420R
- Roussel, H., Helou, G., Hollenbach, D. J., et al. 2007, *ApJ*, 669, 959
- Rubio, M., Lequeux, J., Boulanger, F., et al. 1996, *A&AS*, 118, 263
- Sakamoto, K., Ho, P. T. P., & Peck, A. B. 2006, *ApJ*, 644, 862
- Salomé, P., & Combes, F. 2003, *A&A*, 412, 657
- Sanders, D. B., Scoville, N. Z., & Soifer, B. T. 1991, *ApJ*, 370, 158
- Sandstrom, K. M., Leroy, A. K., Walter, F., et al. 2013, *ApJ*, 777, 5
- Saripalli, L., & Mack, K.-H. 2007, *MNRAS*, 376, 1385
- Savage, B. D., Bohlin, R. C., Drake, J. F., & Budich, W. 1977, *ApJ*, 216, 291
- Schruba, A., Leroy, A. K., Walter, F., et al. 2012, *AJ*, 143, 138
- Scoville, N. Z., Yun, M. S., Sanders, D. B., Clemens, D. P., & Waller, W. H. 1987, *ApJS*, 63, 821
- Smith, J. D. T., Dale, D. A., Armus, L., et al. 2004, *ApJS*, 154, 199
- Smith, J. D. T., Armus, L., Dale, D. A., et al. 2007a, *PASP*, 119, 1133
- Smith, J. D. T., Draine, B. T., Dale, D. A., et al. 2007b, *ApJ*, 656, 770
- Smith, R. J., Glover, S. C. O., Clark, P. C., Klessen, R. S., & Springel, V. 2014, *MNRAS*, 441, 1628
- Snow, T. P., & McCall, B. J. 2006, *ARA&A*, 44, 367
- Solomon, P. M., Rivolo, A. R., Barrett, J., & Yahil, A. 1987, *ApJ*, 319, 730
- Solomon, P. M.; Downes, D.; Radford, S. J. E. & Barrett, J. W. 1997, 478, 144
- Spitzer, L., Jr., & Zweibel, E. G. 1974, *ApJ*, 191, L127

- Spitzer, L., Jr., Cochran, W. D., & Hirshfeld, A. 1974, ApJS, 28, 373
 Spitzer, L., Jr., & Cochran, W. D. 1973, ApJ, 186, L23
 Spitzer, L., Drake, J. F., Jenkins, E. B., et al. 1973, ApJ, 181, L116
 Stierwalt, S., Armus, L., Charmandaris, V., et al. 2014, ApJ, 790, 124
 Strong, A. W., & Mattox, J. R. 1996, A&A, 308, L21
 Tielens, A. G. G. M. 2005, The Physics and Chemistry of the Interstellar Medium, by A. G. G. M. Tielens, pp. . ISBN 0521826349. Cambridge, UK: Cambridge University Press, 2005
 Valentijn, E. A., & van der Werf, P. P. 1999, ApJ, 522, L29
 Veilleux, S., Rupke, D. S. N., Kim, D.-C., et al. 2009, ApJS, 182, 628
 Velusamy, T., & Langer, W. D. 2014, A&A, 572, A45
 Walter, F., Bertoldi, F., Carilli, C., et al. 2003, Nature, 424, 406
 Wolfire, M. G., David Hollenbach., & Christopher, F. McKee. 2010, ApJ, 716, 1191
 Young, L. M., Bureau, M., Davis, T. A., et al. 2011, MNRAS, 414, 940
 Zakamska, N. L. 2010, Nature, 465, 60

TABLE 1
OBSERVED PROPERTIES OF OUR SAMPLE GALAXIES

Galaxy Name (1)	D (Mpc) (2)	Type (3)	L_{IR} ($10^{10} L_{\odot}$) (4)	$\frac{S_{70}}{S_{160}}$ (5)	Ref (6)
N0337	19.3	SF	0.568	0.807	S07
N1097	14.2	SF	2.343	0.932	S07
N1266	31.0	LIN	1.333	1.420	S07
N1291	10.4	LIN	0.039	1.382	S07
N1316	21.0	LIN	0.260	1.368	S07
N1482	22.6	SF	2.812	1.169	S07
N1566	20.4	SY	0.444	0.772	S07
N2798	25.8	SF	2.316	0.407	S07
N2976	3.6	DW	0.007	0.564	S07
N3049	19.2	SF	0.307	1.107	S07
N3184	11.4	SF	0.026	0.604	S07
N3190	19.3	LIN	0.290	0.577	S07
N3198	14.1	SF	0.147	0.813	S07
N3265	19.6	SF	0.237	1.057	S07
Mrk33	22.9	DW	...	1.525	-
N3351	9.3	SF	0.268	0.924	S07
N3521	11.2	LIN	0.266	0.572	S07
N3627	6.4	SY	0.221	1.016	S07
N3938	14.3	SF	0.105	0.436	S07
N4125	23.9	LIN	0.048	0.975	S07
N4254	14.4	SF	0.533	0.602	S07
N4321	14.3	SF	0.513	0.671	S07
N4450	16.5	LIN	0.092	1.116	S07
N4536	14.5	SF	0.905	1.172	S07
N4559	7.00	SF	0.083	0.498	S07
N4569	16.8	LIN	0.426	0.777	S07
N4579	16.4	SY	0.161	0.857	S07
N4625	7.6	DW	0.023	0.518	S07
N4631	9.3	SF	0.306	0.922	S07
N4725	20.5	SY	0.034	0.564	S07
N4736	4.7	LIN	0.115	1.708	S07
N4826	5.3	LIN	0.116	0.782	S07
N5033	14.8	SY	0.577	0.572	S07
N5055	7.9	LIN	0.159	0.557	S07
N5194	7.6	SY	0.308	0.686	S07
N5195	7.6	LIN	0.154	1.652	S07
N5713	21.4	SF	2.998	1.001	S07
N5866	15.3	LIN	0.215	0.981	S07
N6822A	0.5	DW	...	1.151	-
N6946	6.8	SF	0.387	0.958	S07
N7331	14.5	LIN	0.249	0.564	S07
N7552	21.0	SF	5.052	1.244	S07
N7793	3.9	DW	0.009	0.648	S07
3c31	66.7	3C
3c218	240	3C
3c272.1	19.1	3C
3c293	195	3C
3c310	233	3C
3c326n	395	3C
3c424	568	3C
3c433	445	3C
3c436	1016	3C
CenA	11.0	3C
3c236	449	3C
Arp220	77.6	ULI	145	1.678	H06
IRAS 00188-0856	596	ULI	256	...	H06
IRAS 03521+0028	717	ULI	365	...	H06
IRAS 05189-2524	186	ULI	143	2.292	H06
IRAS 06035-7102	356	ULI	166	...	H06
IRAS 06206-6315	418	ULI	169	...	H06
IRAS 07598+6508	700	ULI	337	...	H06
IRAS 08572+3915	258	ULI	137	3.124	H06

TABLE 1 — *Continued*

Galaxy Name (1)	D (Mpc) (2)	Type (3)	L_{IR} ($10^{10} L_{\odot}$) (4)	$\frac{S_{70}}{S_{160}}$ (5)	Ref (6)
IRAS 10565+2448	188	ULI	109	1.362	H06
F12112+0305	324	ULI	212	1.576	H06
IRAS 13451+1232	563	ULI	197	...	H06
F14348-1447	332	ULI	224	1.550	H06
IRAS 17208-0014	188	ULI	250	1.744	H06
IRAS 19254-7245	273	ULI	121	1.468	H06
IRAS 20087-0308	483	ULI	280	...	H06
IRAS 23365+3604	286	ULI	147	1.557	H06
Mrk 273	164	ULI	142	1.899	H06
UGC5101	174	ULI	100	1.053	H06
Mrk 463E	221	ULI	60	...	H06
PG1440+356	347	QSO	42	1.355	E01
N6240	101	LIR	69	1.415	H06
N3110	72.5	LIR	16	0.772	P10
N3256	40.1	LIR	40	1.577	P10
N3690	44.9	LIR	63	1.663	P10
N5135	58.8	LIR	16	1.096	P10
N6701	56.2	LIR	10	0.883	P10
N7130	69.9	LIR	25	1.192	P10
N7591	70.9	LIR	10	0.821	P10
N7771	62.1	LIR	25	0.773	P10

1. Ref: S07 - Smith et al. 2007; K09 - Kennicutt et al. 2009; NED - NASA/IPAC Extragalactic Database; H06 - Higdon et al. 2006; P10 - Pereira Santaella et al. 2010; E01 - Evans et al. 2001
2. Entries in the last column are references for the the infrared luminosity (8-1000 μm), L_{IR} . For SINGS galaxies L_{IR} is calculated using the relation $L_{IR} = 0.94 \times L_{TIR}$ (D. Dale priv. comm.) and the corresponding L_{TIR} values are from Smith et al. (2007a).
3. Distance measurements are from the KINGFISH webpage for SINGS galaxies and for others through NED IPAC Extragalactic Database
4. The S_{70}/S_{160} is the FIR ratio calculated from the PACS 70 and 160 μm fluxes
5. SF: star forming region; LIN: LINERs; SY: Seyferts; DW: Dwarfs; 3C: 3C radio galaxies; ULI: ULIRGs; QSO: Quasar; and LIR: LIRGs
6. The 3c radio galaxies were selected from Ogle et al. (2010).

TABLE 2
OBSERVED MOLECULAR HYDROGEN ROTATIONAL LINE FLUX

Galaxy Name (1)	S(0)(err) (2)	S(1)(err) (3)	S(2)(err) (4)	S(3)(err) (5)	S(4)(err) (6)	S(5)(err) (7)	S(6)(err) (8)	S(7)(err) (9)	M(H ₂) (10 ⁶ M _⊙) (10)
N0337 ^{1,1}	01.16(0.38)	02.10(0.49)	01.54(0.99)	00.97(0.52)	56 (228)
N1097 ^{1,1}	21.31(4.26)	72.61(4.33)	29.36(2.94)	42.30(2.34)	1493
N1266 ^{25,1}	01.64(0.85)	14.85(0.66)	12.18(0.71)	18.98(1.16)	10.27(1.74)	24.19(1.99)	...	19.22(2.86)	1253
N1291 ^{1,1}	00.37(0.18)	02.98(0.48)	01.39(0.82)	03.16(1.00)	9
N1316 ^{1,1}	00.15(0.08)	03.60(0.61)	01.84(0.59)	08.40(0.99)	124
N1482 ^{1,1}	10.68(3.51)	42.40(5.34)	18.40(2.28)	20.75(2.69)	1607
N1566 ^{26,1}	02.40(0.22)	12.95(0.71)	05.53(0.48)	09.16(1.76)	389
N2798 ^{1,1}	04.32(2.53)	20.78(2.21)	09.07(0.92)	10.52(1.21)	273
N2976 ^{1S,1}	00.89(0.24)	01.57(0.30)	00.49(0.35)	00.52(0.42)	1.08 (0.25)
N3049 ^{1,1}	00.64(0.22)	2.37(0.38)	01.17(0.65)	01.11(0.52)	148
N3184 ^{1S,1}	00.98(0.23)	02.26(0.29)	00.63(0.35)	26 (10.6)
N3190 ^{1,1}	01.81(0.29)	07.53(0.80)	02.09(0.64)	07.16(1.26)	110
N3198 ^{1,1}	01.32(0.49)	03.21(0.54)	01.02(0.35)	01.87(0.85)	31
N3265 ^{1,1}	00.93(0.32)	03.06(0.35)	01.14(0.79)	01.53(0.74)	94
Mrk33 ^{1,1}	01.39(0.56)	02.93(0.37)	01.15(0.53)	04.57(0.86)	81
N3351 ^{1S,1}	06.28(1.05)	21.84(2.06)	08.83(1.01)	16.98(1.99)	197 (32)
N3521 ^{1,1}	01.78(0.36)	03.12(0.69)	01.23(0.40)	02.05(0.88)	20
N3627 ^{1S,1}	03.12(0.39)	31.86(1.22)	14.17(0.52)	20.91(1.26)	208 (27)
N3938 ^{1S,1}	00.80(0.12)	01.34(0.33)	00.42(0.32)	37 (30)
N4125 ^{1,1}	00.26(0.16)	01.76(0.47)	01.26(0.64)	01.80(0.88)	26
N4254 ^{1S,1}	01.76(0.13)	08.73(0.95)	04.66(0.92)	03.25(0.88)	342 (700)
N4321 ^{1S,1}	07.82(1.17)	26.75(2.28)	13.21(2.46)	13.21(2.46)	1386 (200)
N4450 ^{1,1}	01.03(0.16)	09.14(0.52)	03.37(0.95)	08.90(1.11)	63
N4536 ^{1S,1}	10.87(3.23)	41.16(4.05)	17.56(2.33)	21.68(2.07)	810 (415)
N4559 ^{1,1}	01.36(0.21)	01.79(0.35)	00.40(0.15)	02.34(1.37)	18
N4569 ^{1,1}	04.16(0.69)	31.61(0.87)	15.24(0.52)	30.94(1.87)	760
N4579 ^{1,1}	00.89(0.23)	16.41(0.52)	10.58(1.24)	25.63(1.00)	205
N4625 ^{1S,1}	00.80(0.16)	00.96(0.19)	00.54(0.43)	8 (21)
N4631 ^{1,1}	05.82(0.64)	12.36(1.61)	06.04(0.50)	04.68(0.91)	73.4
N4725 ^{1S,1}	01.17(0.17)	3.71(0.51)	1.99(0.81)	3.80(0.90)	<170 (<28)
N4736 ^{1S,1}	03.32(0.68)	25.08(1.64)	10.01(1.04)	22.17(1.36)	21 (1.4)
N4826 ^{1,1}	07.13(0.65)	34.53(1.58)	15.09(1.09)	21.06(1.03)	65
N5033 ^{1,1}	03.66(0.35)	18.20(1.04)	06.35(0.31)	12.69(1.91)	190
N5055 ^{1S,1}	04.40(0.24)	15.80(0.91)	05.20(0.67)	08.02(1.06)	87 (20)
N5194 ^{1,1}	01.77(0.28)	13.44(0.91)	07.57(0.47)	18.73(1.77)	32
N5195 ^{1,1}	05.42(2.09)	31.04(1.23)	12.77(0.65)	27.50(1.72)	80
N5713 ^{1S,1}	02.74(0.36)	15.16(1.43)	05.09(0.79)	08.56(0.70)	329 (238)
N5866 ^{1,1}	01.55(0.15)	09.00(0.55)	03.91(0.70)	03.72(0.65)	81
N6822A ^{1,1}	00.81(0.43)	02.11(0.43)	01.60(0.41)	02.59(0.38)	0.03
N6946 ^{1S,1}	22.77(6.19)	63.69(3.35)	27.16(1.71)	28.63(2.93)	346 (32)
N7331 ^{1,1}	01.64(0.16)	04.96(0.50)	01.38(0.19)	02.34(0.83)	120
N7552 ^{1,1}	25.78(10.69)	56.53(4.26)	24.59(2.25)	31.59(1.48)	1950
N7793 ^{1,1}	00.70(0.17)	01.50(0.32)	01.17(0.46)	00.53(0.37)	3
3c031 ^{2,8}	00.64(0.11)	01.36(0.58)	00.59(0.15)	0.60(0.17)	00.76(0.27)	00.80(0.18)	695
3c218 ^{2,9}	00.55(0.11)	00.41(0.22)	00.23(0.09)	00.55(0.08)	00.42(0.15)	00.23(0.05)	...	0.16(0.05)	1895
3c272 ^{1,2,10}	00.42(0.14)	00.55(0.29)	00.27(0.15)	01.40(0.20)	...	01.00(0.40)	01.60(0.40)	...	1.8
3c293 ^{2,11}	01.60(0.20)	05.30(0.40)	01.94(0.07)	03.25(0.07)	01.20(0.10)	02.80(0.20)	00.31(0.11)	1.30(0.10)	14450
3c310 ²	00.12(0.06)	00.36(0.07)	00.08(0.04)	00.48(0.04)	00.19(0.06)	00.29(0.09)	...
3c326n ^{2,12}	00.30(0.06)	00.69(0.06)	00.41(0.04)	01.26(0.05)	00.31(0.06)	00.46(0.22)	00.25(0.09)	00.29(0.09)	1183
3c424 ^{2,13}	00.45(0.07)	01.12(0.06)	00.21(0.03)	00.43(0.04)	00.15(0.04)	00.17(0.07)	...	00.28(0.05)	<3560
3c433 ^{2,14}	02.00(0.40)	01.40(0.20)	00.58(0.17)	01.20(0.20)	...	01.60(0.50)	...	01.20(0.30)	<5495
3c436 ²	00.48(0.16)	00.46(0.07)	00.31(0.12)	00.28(0.04)	...	00.22(0.10)	00.41(0.12)	00.21(0.10)	...
CenA ^{2,15}	10.00(6.00)	57.00(9.00)	27.00(4.00)	09.30(3.70)	...	12.00(3.00)	...	27.00(4.00)	<210
3c236 ^{3,10}	00.20(0.03)	00.95(0.07)	00.32(0.05)	00.64(0.05)	<6220
Arp220 ^{4,16}	< 970	18.62(1.68)	09.80(1.30)	07.30(0.20)	12.90(3.80)	22500
IRAS 00188-0856 ^{4,16}	< 19	00.43(0.05)	00.20(0.04)	00.38(0.12)	< 32	21300
IRAS 03521+0028 ^{4,16}	< 13	00.82(0.13)	00.27(0.09)	00.37(0.03)	< 3.0	29400
IRAS 05189-2524 ^{4,16}	< 282	03.40(0.70)	01.50(0.20)	03.60(1.30)	< 341	3200
IRAS 06035-7102 ^{4,17}	< 61	04.17(0.04)	02.33(0.58)	03.4(1.00)	< 116	19000
IRAS 06206-6315 ^{4,17}	< 29	01.29(0.10)	00.50(0.05)	00.59(0.19)	< 18	41400
IRAS 07598+6508 ^{4,16}	< 30	01.38(0.70)	00.37(0.06)	00.67(0.02)	< 225	36000
IRAS 08572+3915 ^{4,16}	< 154	01.19(0.04)	00.51(0.10)	00.46(0.13)	< 430	4200
IRAS 10565+2448 ^{4,16}	< 109	06.57(0.05)	02.56(0.09)	04.03(0.02)	< 54	17900
F12112+0305 ^{4,18}	1.4(0.4)	4.12(0.44)	1.73(0.31)	2.37(0.03)	4.10(0.8)	19200
IRAS 13451+1232 ^{4,18}	< 45	02.83(0.65)	01.29(0.05)	02.19(0.26)	< 41	<46900
F14348-1447 ^{4,18}	< 6.1	4.47(0.15)	1.95(0.10)	2.4(0.21)	< 31	20500
IRAS 17208-0014 ^{4,16}	< 239	08.81(0.09)	04.97(0.85)	05.7(1.1)	< 85	22400

TABLE 2 — *Continued*

Galaxy Name (1)	S(0)(err) (2)	S(1)(err) (3)	S(2)(err) (4)	S(3)(err) (5)	S(4)(err) $10^{-17} \text{ W m}^{-2}$ (6)	S(5)(err) (7)	S(6)(err) (8)	S(7)(err) (9)	M(H ₂) (10 ⁶ M _⊙) (10)
IRAS 19254-7245 ^{4,17}	< 85	08.81(0.57)	03.82(0.95)	03.82(0.04)	< 4.00	21000
IRAS 20087-0308 ^{4,16}	< 21	02.29(0.14)	00.84(0.33)	01.3(0.40)	< 22	51100
IRAS 23365+3604 ^{4,16}	< 91	03.9(0.31)	02.01(0.95)	03.1(0.5)	< 30	27000
Mrk 273 ^{4,16}	< 262.5	10.24(0.09)	05.6(0.70)	10.4(0.9)	< 150	15870
UGC5101 ^{4,19}	< 100	04.96(0.47)	02.7(0.5)	02.8(0.30)	< 195	7500
Mrk463E ^{4,18}	< 79	02.79(0.37)	01.31(0.08)	02.8(0.60)	< 385	2180
PG1440+356 ^{5,20}	0.60(0.14)	1.14(0.14)	0.51(0.06)	0.64(0.11)	6400
N6240 ^{6,21}	8.60(1.20)	50.40(1.50)	39.8(0.50)	70.90(1.90)	36.4(10.8)	95.2(16.6)	...	33.7(12.5)	14100
N3110 ^{7,21}	1.60(0.20)	10.00(0.90)	4.00(1.00)	5750
N3256 ^{7,22}	9.00(3.00)	61.0(5.00)	34.0(3.00)	1400
N3690 ^{7,21}	3.80(0.60)	22.0(1.00)	11.0(4.00)	3700
N5135 ^{7,21}	1.30(0.50)	17.00(1.00)	9.30(1.40)	5500
N6701 ^{7,21}	1.90(0.90)	10.00(1.00)	4.60(0.80)	1200
N7130 ^{7,23}	1.40(0.30)	09.90(0.70)	4.20(1.70)	4130
N7591 ^{7,24}	1.00(0.30)	05.50(0.60)	3.00(1.00)	3270
N7771 ^{7,21}	3.50(1.80)	16.00(1.00)	8.70(1.20)	3280

1. The cold H₂ gas mass is calculated using $\alpha_{\text{CO,Gal}} = 3.2 \text{ M}_{\odot} (\text{K km s}^{-1} \text{ pc}^2)^{-1}$ (not considering Helium and other heavy element mass contribution)

2. The mass value in the parentheses is calculated using CO weighted mean α_{CO} , suggested by Sandstrom et al. (Table 4) 2013 using a constant dust to gas ratio (DGR) marked in the reference as “S”

3. The two numbers as the notemark in the first column of the table correspond to references. The first number is the reference from which we adopt the MIR H₂ rotational line flux and the second number is for the cold H₂ gas mass derived from the CO emission.

Ref: (1) Roussel et al. 2007; (1S) Sandstrom et al.2013 + Roussel et al. 2007; (2) Ogle et al. 2010; (3) Guillard et al. 2012; (4) Hiqdon et al. 2006; (5) QUEST sample by S. Veilleux (2009); (6) Armus et al. 2006; (7) M. Pereira-Santaella. 2010; (8) Okuda et al. 2005; (9) Salome & Combes 2003; (10) Ocaña Flaquer et al. 2010; (11) Evans et al. 1999; (12) Nesvadba et al. 2010; (13) Saripalli & Mack 2007; (14) Evans et al. 2005; (15) Israel et al. 1990; (16) Solomon et al. 1997; (17) Mirabel et al. 1989; (18) Evans et al. 2002; (19) Rigopoulou 1996; (20) Evans et al. 2001; (21) Sanders et al. 1991; (22) Kazushi Sakamoto et al. (2006); (23) Curran et al. (2000); (24) Lavezzi & Dickey 1998; (25) Young et al. (2011); (26) Harnett et al.(1991)

TABLE 3
OBSERVED MOLECULAR HYDROGEN LINES

Transition $\nu = 0$ (1)	Short notation (2)	Rest λ (μm) (3)	$\frac{E_u}{k}$ (K) (4)	A (10^{-11}s^{-1}) (5)
$J = 2 \rightarrow 0$	S(0)	28.219	0510	2.95
$J = 3 \rightarrow 1$	S(1)	17.035	1015	47.6
$J = 4 \rightarrow 2$	S(2)	12.279	1681	275.0
$J = 5 \rightarrow 3$	S(3)	9.665	2503	980.0
$J = 6 \rightarrow 4$	S(4)	8.025	3473	2640.0
$J = 7 \rightarrow 5$	S(5)	6.910	4585	5880.0
$J = 8 \rightarrow 6$	S(6)	6.109	5828	11400.0
$J = 9 \rightarrow 7$	S(7)	5.511	7196	20000.0

NOTE. — The rotational upper level energies were computed from the molecular constants given by Huber (1979) and transition probabilities are from Black & Dalgarno (1976)

TABLE 4
MODEL DERIVED PARAMETERS FOR SINGS
GALAXIES

Galaxy Name (1)	T_ℓ (K) (2)	n (3)	$\frac{M(T > 100K)}{M_{\text{total}}}$ (in %) (4)
N0337	59 (43)	5.47	9.46 (2.3)
N1097	47	5.00	4.88
N1266	26	3.80	2.30
N1291	52	4.27	11.79
N1316	30	3.79	3.48
N1482	51	5.00	6.76
N1566	42	3.89	8.15
N2798	71	4.96	25.76
N2976	66 (89)	5.87	13.22 (56.6)
N3049	42	5.02	3.06
N3184	57 (69)	5.57	7.67 (18.3)
N3190	55	4.68	11.08
N3198	60	5.20	11.70
N3265	53	5.15	7.17
Mrk33	43	4.28	6.28
N3351	43 (70)	4.75	4.22 (26.2)
N3521	63	5.42	12.97
N3627	43 (77)	4.53	5.08 (39.7)
N3938	57 (55)	6.00	6.02 (5.03)
N4125	50	4.16	11.18
N4254	35 (29)	4.68	2.10 (1.05)
N4321	38 (62)	4.96	2.18 (15.1)
N4450	53	4.28	12.46
N4536	49 (58)	5.03	5.64 (11.1)
N4559	51	5.90	3.69
N4569	37	4.30	3.76
N4579	37	3.92	5.48
N4625	65 (54)	6.39	9.81 (3.61)
N4631	51	5.25	5.72
N4725	> 51	4.79	< 7.8
N4736	52 (112)	4.54	9.88 (149)
N4826	50	4.85	6.93
N5033	51	4.65	8.56
N5055	50 (72)	5.05	6.04 (26.4)
N5194	39	3.94	6.28
N5195	50	4.51	8.78
N5713	56 (61)	4.91	10.36 (14.5)
N5866	55	4.70	10.95
N6822A	39	4.20	4.91
N6946	45 (82)	4.96	4.23 (45.6)
N7331	49	5.21	4.96
N7552	51	5.02	6.67
N7793	48	5.25	4.42

NOTE. — The value in the parentheses is calculated assuming central α_{CO} from the dust emission, evaluated by Sandstrom et al. 2013

TABLE 5
MODEL DERIVED PARAMETERS FOR RADIO, U/LIRGS GALAXIES

Galaxy Name (1)	Ref (2)	Model mass ($10^6 M_\odot$) (3)	T_ℓ (K) (4)	n (5)	$\frac{M(T>100K)}{M_{total}}$ (in %, for T_ℓ) (6)	T'_ℓ (K) (7)	$\frac{M(T>100K)}{M_{total}}$ (in %, for T'_ℓ) (8)
3c031	1	360	41	4.69	3.73	65	20.40
3c218	1	1040	41	4.47	4.53	67	24.92
3c272.1	1	1.87	50	3.41	18.8	101	102.4
3c293	1	13210	48	4.77	6.28	75	33.81
3c310	1	515	...	4.11
3c326n	1	2604	64	4.05	25.0	112	126.2
3c424	1	40820	>88	5.19	>58.5	>132	>320.0
3c433	1	12850	>62	4.51	>18.7	>101	>103.6
3c436	1	18820	...	4.40
CenA	1	379	>58	4.64	>13.8	>93	>76.79
3c236	2	14083	>61	4.86	>14.8	>95	>82.04
Arp220	3	10000	41	5.07	2.65	62	14.13
IRAS 00188-0856	3	5472	33	4.38	2.36	55	13.13
IRAS 03521+0028	3	53970	57	5.35	8.67	84	48.02
IRAS 05189-2524	3	3600	52	4.27	11.8	87	62.94
IRAS 06035-7102	3	19240	50	4.39	9.54	82	51.55
IRAS 06206-6315	3	11760	36	4.68	2.33	56	11.80
IRAS 07598+6508	3	76700	60	5.27	11.3	88	58.93
IRAS 08572+3915	3	6586	53	5.02	7.80	85	51.64
IRAS 10565+2448	3	19746	51	5.04	6.60	78	35.82
IRAS 12112+0305	3	38640	59	5.07	11.7	90	63.80
IRAS 13451+1232	3	43890	>49	4.57	>7.83	>78	>41.27
IRAS 14348-1447	3	37130	59	4.74	13.9	92	72.38
IRAS 17208-0014	3	14900	45	4.59	5.69	71	29.40
IRAS 19254-7245	3	89760	69	5.42	19.4	101	106.48
IRAS 20087-0308	3	45390	49	5.03	5.64	74	28.89
IRAS 23365+3604	3	18230	45	4.72	5.13	71	27.30
Mrk 273	3	9730	43	4.37	5.82	71	31.55
UGC5101	3	11655	56	4.96	10.1	85	53.17
Mrk 463E	3	4320	61	4.24	19.7	102	107.1
PG1440+356	4	11735	58	5.04	11.1	88	59.58
N6240	5	7240	40	3.73	8.20	65	30.95
N3110	5	1520	33	4.22	2.82	51	11.33
N3256	5	1360	50	3.71	15.3
NGC3690/IC694	5	1310	36	4.04	4.48	56	17.21
N5135	5	820	25	3.70	25.2	41	9.17
N6701	5	800	44	4.13	7.65	68	30.36
N7130	5	1320	35	4.18	3.55	54	14.13
N7591	5	754	32	4.18	2.67	49	10.17
N7771	5	1000	33	3.82	4.39	54	17.25

NOTE. — 1. The molecular gas mass in column 3 is calculated extrapolating the power law model to $T_\ell^* = 49$ K.

2. The temperature in column 4 is the model extrapolated temperature required to fit the total molecular gas mass, calculated using the $\alpha_{CO,Gal}$.

3. The warm gas mass fraction listed in column 6 is derived using the cold molecular gas mass by assuming $\alpha_{CO,Gal}$.

4. The temperature in column 7 is the model extrapolated temperature required to fit the total molecular gas mass assuming a low α_{CO} of $0.8 M_\odot (K \text{ km s}^{-1} \text{ pc}^2)^{-1}$.

5. The warm gas mass fraction listed in column 8 is derived using the cold molecular gas mass by assuming a low α_{CO} .

Table 6
Observed molecular hydrogen line fluxes and mass in low metallicity dwarfs

Galaxy Name	12+log[O/H] ^a	S(0)	S(1)	S(2)	S(3)	S(4)	S(5)	D	M(H ₂ ,CO) ^c	M(H ₂ ,dust) ^d	M(H ₂ ,model)	n
(1)	(2)	(3)	(4)	(5)	(6)	(7)	(8)	(9)	(10)	(11)	(12)	(13)
CG007-025 ^b	7.77	...	5.45(0.43)	1.67(0.43)	...	0.72(0.21)	...	24.5	41.2	...	3935	5.24
N66	8.10	475(181)	1025(116)	1283(175)	433(207)	586(400)	482(314)	0.06	0.016	0.435	0.451	3.59
Haro 11	8.20	<2.49	1.68(0.55)	1.01(0.13)	1.21(0.18)	92	1670	4500 ^e	6700	4.52
UM311	8.31	...	1.49(0.69)	0.73(0.35)	0.66(0.27)	24	95	...	400	4.51
HubbleV	8.42	0.81(0.43)	2.11(0.43)	1.60(0.41)	2.59(0.38)	0.5	0.27	0.28	0.16	4.20

a. Ref for metallicity CGCG 007-025:Izotov et al. (2007); N66:Dufour et al. (1982); Dufour (1984); Haro 11:Guseva et al. (2012); UM 311:Izotov & Thuan (1998); and HubbleV:Peimbert et al. (2005)

b. For CGCG 007-025 we also used the S(7) line flux of H₂, $(0.46 \pm 0.13) \times 10^{-17} \text{ W m}^{-2}$, from Hunt et al. (2010)

c. Ref for CO derived H₂ mass CGCG 007-025:Hunt et al. (2015); N66:Rubio et al. (1996); Haro 11 and UM 311:Cormier et al. (2014); HubbleV:Israel et al. (2003)

d. Ref for dust derived H₂ mass N66:Leroy et al. (2007); Haro11:Cormier et al. (2014); HubbleV:Israel et al. (1996)

e. The molecular gas mass for Haro11 is in the range $(4.5\text{--}11.5) \times 10^8 \text{ M}_\odot$, due to uncertainty in HI mass. In the table we mention the minimum value